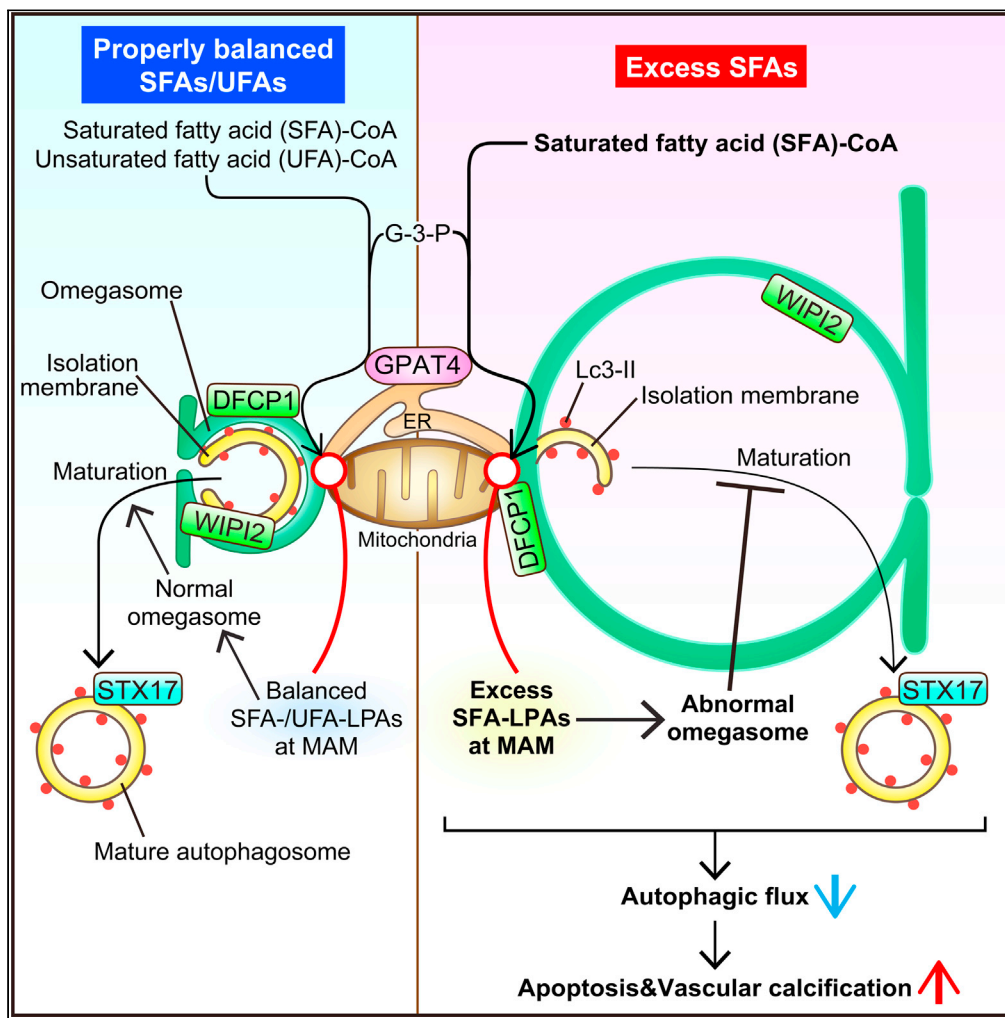


Article

GPAT4-Generated Saturated LPAs Induce Lipotoxicity through Inhibition of Autophagy by Abnormal Formation of Omegasomes



Yuji Shiozaki,
Shinobu Miyazaki-
Anzai, Kayo
Okamura, Audrey
L. Keenan,
Masashi Masuda,
Makoto Miyazaki

makoto.miyazaki@cuanschutz.
edu

HIGHLIGHTS

SMC-specific autophagy
deficiency aggravates
vascular calcification in
CKD

SFAs block autophagy by
accumulating saturated
LPAs in MAM via GPAT4

SFA-LPAs induce
abnormal omegasome
formation and isolation
membrane accumulation

UFA-LPAs attenuate SFA-
induced abnormal
omegasome formation
and vascular calcification

Shiozaki et al., iScience 23,
101105
May 22, 2020 © 2020 The
Author(s).
[https://doi.org/10.1016/
j.isci.2020.101105](https://doi.org/10.1016/j.isci.2020.101105)



Article

GPAT4-Generated Saturated LPAs Induce Lipotoxicity through Inhibition of Autophagy by Abnormal Formation of Omegasomes

Yuji Shiozaki,¹ Shinobu Miyazaki–Anzai,¹ Kayo Okamura,¹ Audrey L. Keenan,¹ Masashi Masuda,¹ and Makoto Miyazaki^{1,2,*}

SUMMARY

Excessive levels of saturated fatty acids are toxic to vascular smooth muscle cells (VSMCs). We previously reported that mice lacking VSMC-stearoyl-CoA desaturase (SCD), a major enzyme catalyzing the detoxification of saturated fatty acids, develop severe vascular calcification from the massive accumulation of lipid metabolites containing saturated fatty acids. However, the mechanism by which SCD deficiency causes vascular calcification is not completely understood. Here, we demonstrate that saturated fatty acids significantly inhibit autophagic flux in VSMCs, contributing to vascular calcification and apoptosis. Mechanistically, saturated fatty acids are accumulated as saturated lysophosphatidic acids (LPAs) (i.e. 1-stearoyl-LPA) possibly synthesized through the reaction of GPAT4 at the contact site between omegasomes and the MAM. The accumulation of saturated LPAs at the contact site causes abnormal formation of omegasomes, resulting in accumulation of autophagosomal precursor isolation membranes, leading to inhibition of autophagic flux. Thus, saturated LPAs are major metabolites mediating autophagy inhibition and vascular calcification.

INTRODUCTION

Vascular calcification is a major complication in aging populations and patients with chronic kidney disease (CKD), who display characteristics of premature aging (Kovacic et al., 2011a, 2011b; Liu et al., 2013; Shannah et al., 2011). Vascular calcification is highly associated with cardiovascular mortality (Blacher et al., 2001; Block et al., 2007). Recent studies revealed that saturated fatty acids (SFAs) contribute to the development of vascular calcification by promoting vascular apoptosis and transdifferentiation of vascular smooth muscle cells (VSMCs) to osteoblastic-like cells (Durham et al., 2018; Proudfoot et al., 2000). “Lipotoxicity” of excess SFAs is manifested as apoptosis, endoplasmic reticulum (ER) stress, or production of oxidative stress that accelerates vascular calcification (Anderson et al., 2012; Brodeur et al., 2013; Masuda et al., 2012). Stearoyl-CoA desaturase (SCD) catalyzes the conversion of SFAs to unsaturated fatty acids (UFAs) by introducing a double bond at the $\Delta 9$ position (Miyazaki and Ntambi, 2003). In our previous *in vivo* and *in vitro* studies, SCD inhibition induced vascular calcification and cell apoptosis associated with excess accumulation of metabolites of SFAs in VSMCs (Masuda et al., 2015). Using lipidomic and shRNA screening approaches, we identified three acyltransferases, glycerol-3-phosphate acyltransferase-4 (GPAT4), and acylglycerol-3-phosphate acyltransferase-3 and -5 (AGPAT3 and AGPAT5), that mediate SFA-induced ER stress and vascular calcification by generating fully saturated phosphatidic acids (PAs) such as distearoyl-phosphatidic acid in VSMCs. Importantly, two recent bias studies have confirmed our observations that GPAT4 is a central enzyme mediating SFA-induced global cellular lipotoxicity (Piccolis et al., 2019; Zhu et al., 2019). However, whether other lipotoxic pathways and other SFA metabolites generated through GPAT4 contribute to vascular calcification is still obscure.

The autophagy-related gene (ATG) family generates the autophagosome membrane (Dikic and Elazar, 2018; Mizushima and Komatsu, 2011). During the activation state of autophagy, the phosphatidylinositol 3-kinase VPS34 and Beclin-1 complex is recruited to the ER-mitochondria contact site, the mitochondria-associated membrane (MAM) (Hamasaki et al., 2013), and generates phosphatidylinositol 3-phosphate (PI3P) as an early event of autophagy (Itakura et al., 2008; Matsunaga et al., 2009; Sun et al., 2008; Zhong et al., 2009). PI3P-enriched ER membrane, known as the origin for autophagosome membrane formation,

¹Division of Renal Diseases and Hypertension, University of Colorado-Denver, Aurora, CO, USA

²Lead Contact

*Correspondence: makoto.miyazaki@cuanschutz.edu

<https://doi.org/10.1016/j.isci.2020.101105>



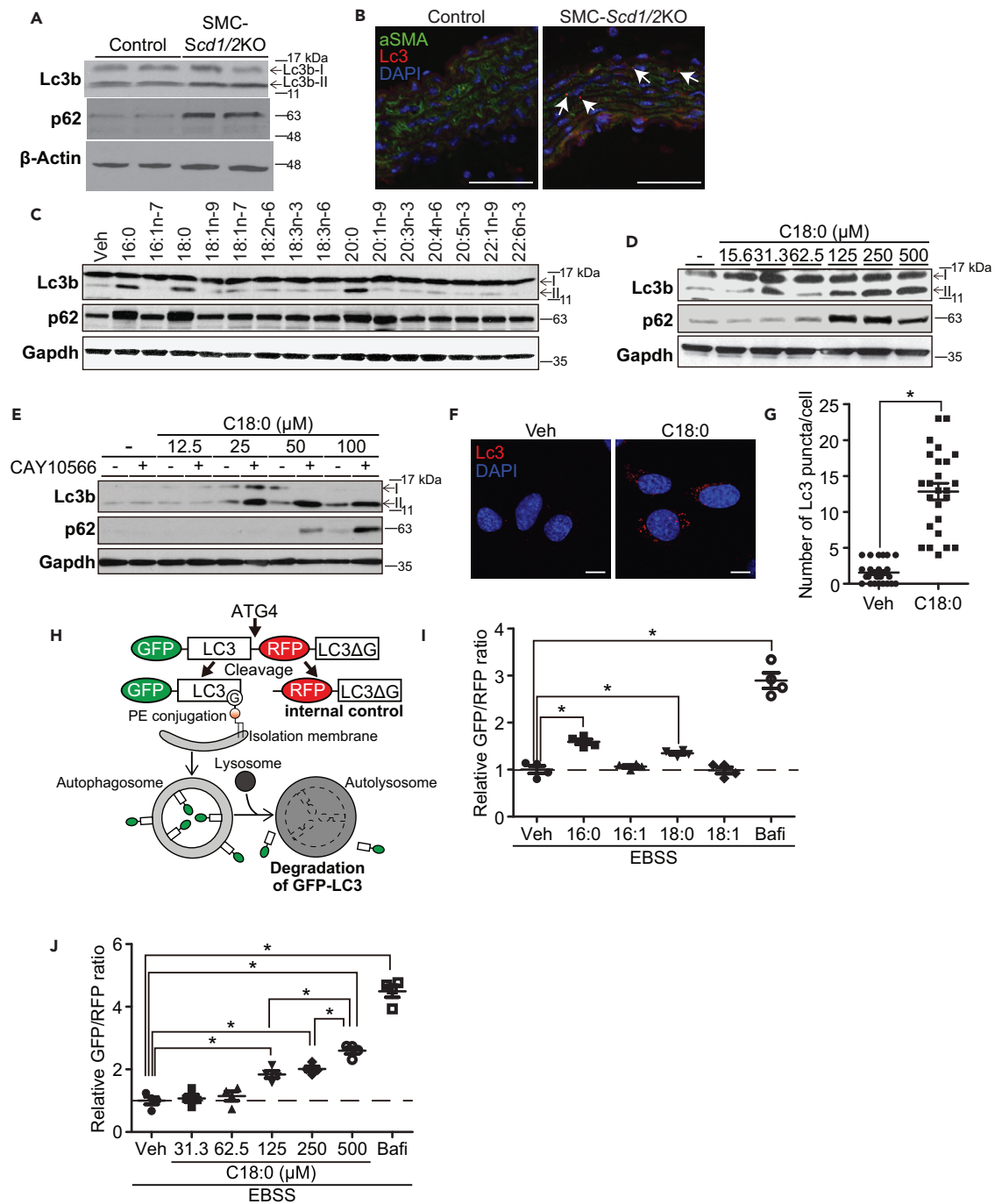


Figure 1. Saturated Fatty Acids (SFAs) Inhibited Autophagic Flux in Mouse Models and Cultured Vascular Smooth Muscle Cells (VSMCs)

(A) Immunoblot analysis of aortic media of control and smooth muscle cell (SMC)-specific *Scd1/2* knockout (KO) mice.
 (B) Confocal microscopy merged images of alpha-smooth muscle actin (aSMA, green), Lc3 (red), and DAPI (blue) in aortas of control and SMC-*Scd1/2* KO mice with CKD. Scale represents 50 μ m. Arrow indicates Lc3 punctation.
 (C) Immunoblot analysis of human VSMCs treated with 250 μ M of 15 major saturated or unsaturated fatty acids for 6 h.
 (D) Dose-dependent effect of C18:0 (SFA) on Lc3b and p62 proteins. Immunoblot analysis of VSMCs treated with C18:0 for 6 h.
 (E) Immunoblot analysis of VSMCs treated with C18:0 and 3 μ M CAY10566 for 6 h.
 (F) Immunofluorescence of Lc3 (red) and DAPI (blue) in VSMCs treated with vehicle or 200 μ M C18:0 for 2 h.
 (G) Number of Lc3 puncta in Figure 1F (n = 25, 2-tailed Student's t test). *p < 0.05. Data are represented as mean \pm SEM.
 (H) Scheme of measurement of autophagic flux with GFP-LC3-RFP-LC3 Δ G probe.

Figure 1. Continued

(I) Measurement of autophagic flux using stable VSMCs expressing GFP-LC3-RFP-LC3ΔG co-treated with Veh, 300 μM C16:0, C16:1, C18:0, C18:1, or 200 nM bafilomycin A1 under EBSS conditions for 6 h. GFP/RFP ratio data were expressed as fold value against Veh (n = 4, One-way ANOVA). *p < 0.05.

(J) Measurement of autophagic flux in stable VSMCs expressing GFP-LC3-RFP-LC3ΔG treated with C18:0 or bafilomycin A1 under EBSS conditions for 6 h (n = 4).

can be visualized by specific PI3P-binding proteins such as double FYVE domain-containing protein-1 (DFCP1) and WD repeat domain phosphoinositide-interacting protein-2 (WIPI2), which are positive membranes called “omegasomes” whose structure is shaped as the letter “Ω” (Axe et al., 2008; Polson et al., 2010). Omegasomes are a platform to form isolation membranes (an autophagosomal precursor) that are unclosed autophagosome membrane structures visualized by either LC3 or ATG16L1 in combination with omegasome markers such as WIPI2 and DFCP1 (Axe et al., 2008; Itakura and Mizushima, 2010; Polson et al., 2010). When the omegasome structure is deformed by inhibition of the capping protein (CapZ)-dependent actin filament assembly, the abnormal isolation membrane structure accumulates DFCP1-positive elongated membrane structures (Mi et al., 2015). However, metabolites that can affect the omegasome structure are still not identified. LC3 is conjugated to the PE molecule on the isolation membrane as lipidated LC3 (LC3-II) by the ATG12-ATG5-ATG16 complex, similar to ubiquitin conjugation after cleavage of glycine 120 residue of LC3 by ATG4 (Fujita et al., 2008; Ichimura et al., 2000; Kabeya et al., 2004; Matsushita et al., 2007; Mizushima et al., 2003; Tanida et al., 2004). The isolation membrane matures to an autophagosome with a double membrane structure while loading autophagic cargo such as Sequestosome-1 (p62) or damaged mitochondria (Dikic and Elazar, 2018; Yoshii and Mizushima, 2017). The mature autophagosome then fuses with a lysosome to generate autolysosomes for degradation inside of Lc3-II and cargo proteins (Gatica et al., 2018; Lamark et al., 2017). Inhibition of autophagy machinery such as an autophagosome-lysosome fusion or protein degradation in autolysosomes induces accumulation of Lc3-II and autophagic substrates (Yoshii and Mizushima, 2017). Because a number of membrane formations and modulations are involved in autophagy machinery, phospholipid modulations such as PI3P and PE are known to affect autophagic flux (Mitroi et al., 2017; Petiot et al., 2000; Rockenfeller et al., 2015). Besides their role in phospholipids, fatty acyl chains are involved in autophagic machinery. For instance, SCD contributes to autophagosome formation at an early stage of autophagy initiation through an unknown mechanism (Ogasawara et al., 2014). In addition, there are a number of studies showing that saturated and unsaturated fatty acids (SFAs and UFAs) modulate autophagy (Choi et al., 2009; Las et al., 2011; Mei et al., 2011; Tan et al., 2012), although a precise conclusion has not been made due to the lack of a detailed mechanistic study. In addition, emerging evidence suggests that the modulation of autophagy contributes to lipotoxicity-mediated diseases such as vascular calcification (Leidal et al., 2018; Levine and Kroemer, 2008; Nussenzweig et al., 2015; Rogers and Aikawa, 2019; Ueno and Komatsu, 2017). Inhibition of autophagy by phosphatidylinositol 3-kinase (PI3K) inhibitor worsens inorganic phosphate (Pi)-induced vascular calcification through secretion of matrix vesicles with alkali phosphatase (Dai et al., 2013), whereas an activator of autophagy, rapamycin, inhibits vascular calcification (Zhao et al., 2015). CKD induces the accumulation of aortic Lc3-II (Dai et al., 2013). However, there is no direct evidence that autophagy plays a causative or protective role in regulating vascular calcification *in vivo*.

In this study, we present evidence that SFA-mediated autophagy inhibition contributes to lipotoxicities including vascular calcification and apoptosis and identify the mechanisms by which SFAs mediate autophagic flux.

RESULTS**Saturated Fatty Acids Induced Accumulation of Lipidated Lc3 and p62 in Mouse Aortas and Cultured Vascular Smooth Muscle Cells**

Smooth muscle cell (SMC)-specific SCD1/2 deficiency induced severe medial calcification, consistent with our previous report (Masuda et al., 2015) (Figure S1A and S1B). Because recent studies suggest that autophagy contributes to vascular calcification, we examined levels of Lc3b-II and p62 proteins in the aortas from SMC-*Scd1/2* knockout (KO) mice by immunoblot analysis (Figure 1A). *Scd1/2* KO induced accumulation of lipidated Lc3b (Lc3b-II) and p62 proteins. Immunofluorescence analysis revealed a significant increase in Lc3 punctation in the aortas of SMC-*Scd1/2* KO mice (Figure 1B). In addition, another mouse model with vascular calcification, mice with 5/6 nephrectomy (Figure S1C), also had significantly higher protein levels of the aortic autophagy substrates Lc3b-II and p62 than sham-operated control mice (Figure S1D). These results suggest that SMC-specific *Scd1/2* KO and CKD modulate autophagic flux *in vivo*.

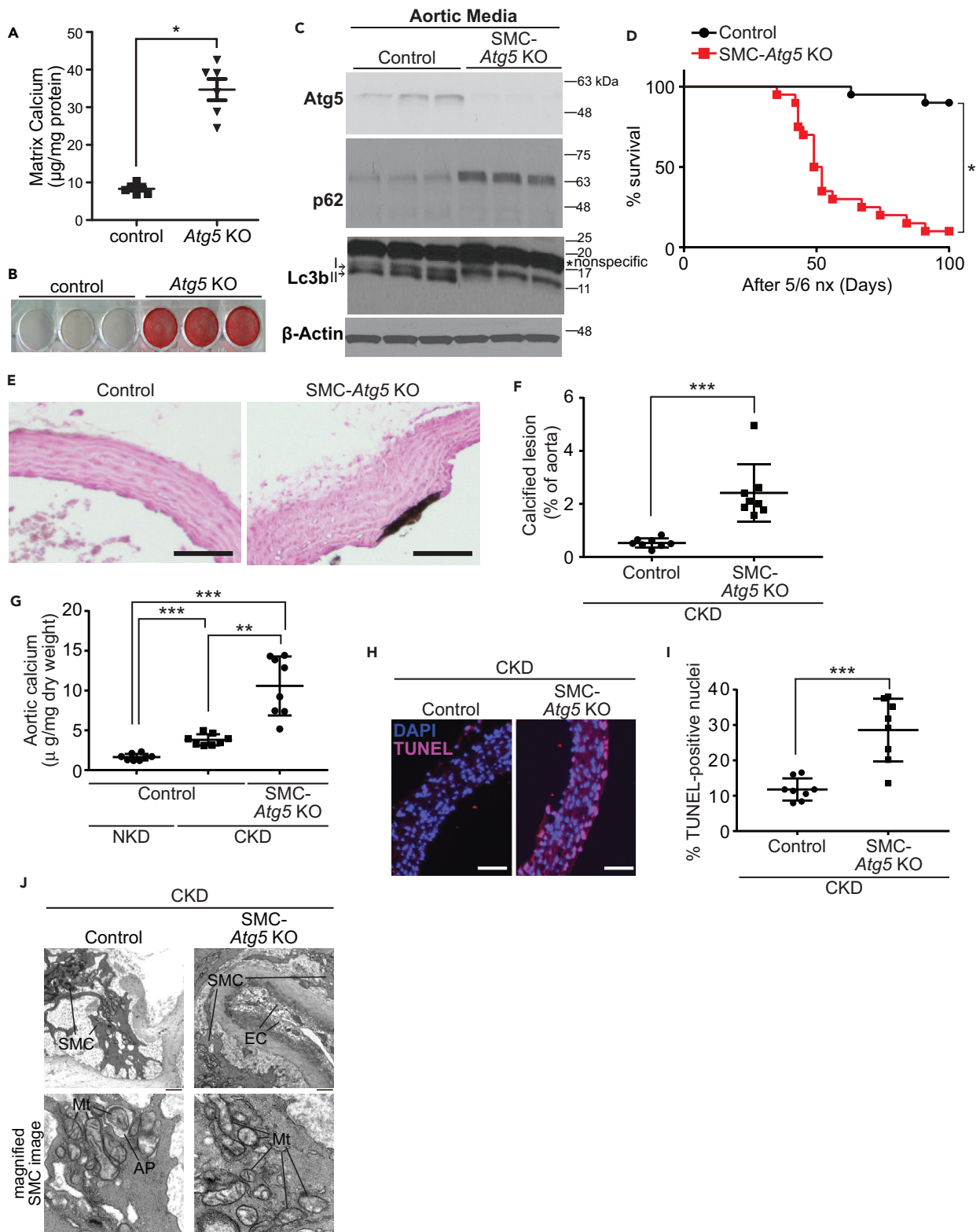


Figure 2. Deficiency of Atg5-Dependent Autophagy in Smooth Muscle Cells (SMCs) Induced Death at a High Mortality Rate, Severe Calcification, and Apoptosis in 5/6 Nephrectomized Mice

- (A) Mineralization of scrambled sg (control) or *Atg5* knockout (KO) VSMCs treated with 2.6 mM Pi every 2 days for 6 days. (n = 6, 2-tailed Student's t test) *p < 0.05. Data are represented as mean ± SEM.
- (B) Alizarin red staining of control and *Atg5* knockout VSMCs treated with Pi for 6 days.
- (C) Immunoblot analysis of aortic medias from control and SMC-*Atg5* KO mice.
- (D) Survival rate of control and SMC-*Atg5* KO mice after 5/6 nephrectomy (n = 20, log rank and Wilcoxon signed rank method) *p < 0.05.
- (E) Photograph (x10 magnification) of the lesions of aortic sinuses with von Kossa staining in control and SMC-*Atg5* KO mice with CKD. Scale represents 50 μm.
- (F) Quantitative analysis of aortic calcified regions (n = 8, 2-tailed Student's t test). ***p < 0.001. Data are represented as mean ± SEM.
- (G) Aortic calcium content (n = 8, one-way ANOVA). **p < 0.01, ***p < 0.001. Data are represented as mean ± SEM.
- (H) Photograph of TUNEL staining (magenta) and DAPI (blue) from aortas of control and SMC-*Atg5* KO mice with CKD. Scale represents 50 μm.
- (I) Quantitative analysis of TUNEL-positive nuclei in aortic lesions (n = 8, 2-tailed Student's t test). ***p < 0.001. Data are represented as mean ± SEM.
- (J) Electron micrograph of aortic lesions in control and SMC-*Atg5* KO mice with CKD. Scale represents 1 μm. SMC, smooth muscle cells; EC, endothelial cells; AP, autophagosome; Mt, mitochondria.

To examine the effect of fatty acids on autophagy in VSMCs, we treated VSMCs with 15 major fatty acids in mammals and analyzed levels of Lc3b and p62 proteins under nutrient-rich (complete media) and starvation (EBSS) conditions (Figures 1C and S1E). SFAs such as palmitic (C16:0), stearic (C18:0), and arachidic (C20:0) acids but no unsaturated fatty acids (UFAs) induced accumulation of Lc3b-II and p62. Levels of Lc3b-II and p62 were dose-dependently increased by treatment with C18:0 under both nutrient-rich and starvation (EBSS) conditions (Figure 1D and S1F). Treatment with CAY10566 (an SCD-specific inhibitor) potentiated the effect of C18:0 on autophagy in VSMCs (Figure 1E). Consistent with the immunoblot analysis, treatment of VSMCs with C18:0 significantly increased the number of Lc3 puncta (Figures 1F and 1G). In addition, GFP-p62-stable VSMCs treated with SFAs and SCD inhibitor but not UFAs significantly induced accumulation of GFP-p62 puncta (Figures S1G and S1H). Similar to VSMCs, treatment with C18:0 in various cell lines such as NIH3T3 and HeLa also induced accumulation of Lc3b-II and p62 (Figures S1I and S1J). To further analyze the effect of SFA-induced autophagy inhibition, we assessed ER-phagy. C18:0 blocked starvation-induced degradation of ER-phagy receptor proteins such as Testis-expressed 264 (Tex264) (An et al., 2019; Chino et al., 2019) and Fam134b (Khaminets et al., 2015; Kohno et al., 2019), accompanied by accumulation of Lc3b-II (Figure S1K).

SFAs Block Autophagic Flux

SFAs induced accumulation of Lc3b-II and p62. Accumulation of Lc3b-II possibly occurs by both induction and inhibition of autophagy. We next examined whether SFAs either induce or inhibit autophagic flux using an autophagy probe, the GFP-LC3-RFP-LC3ΔG probe (Kaizuka et al., 2016). The probe is cleaved by Atg4 under autophagy induction and divided into GFP-LC3 and RFP-LC3ΔG. GFP-LC3 conjugates with PE on an isolation membrane through glycine 120 residue. After autophagosome-lysosome fusion, interior GFP-LC3 is degraded and GFP fluorescence is diminished by the acidic environment of the autolysosome. Because RFP-LC3ΔG cannot be degraded by incapability of conjugation to PE due to deletion of glycine 120, RFP fluorescence can be used as internal control due to its stability. A decline of the GFP/RFP ratio indicates autophagic flux (Figure 1H). To examine the effect of fatty acids on autophagic flux, VSMCs stably expressing GFP-LC3-RFP-LC3ΔG were treated with SFAs and UFAs. Treatment with SFAs such as C16:0 and C18:0 but not UFAs such as C16:1 and C18:1 dose-dependently increased the GFP/RFP ratio compared with vehicle (Figures 1I and 1J). These results conclude that SFAs block autophagic flux, resulting in significant accumulation of autophagic substrates such as Lc3b-II and p62 in VSMCs.

Inhibition of Autophagy Induces Mortality and Vascular Calcification in CKD

Because SFAs inhibit autophagic flux, we next examined whether inhibition of autophagy induces vascular calcification. In VSMC cultures, *Atg5* KO significantly induced mineralization of VSMCs (Figures 2A, 2B, and S2A). We next generated SMC-specific *Atg5* KO mice to study the effect of *Atg5* on the development of autophagy in CKD *in vivo*. The deletion of the gene of interest was observed in smooth muscle cells but no other cells, as previously reported (Figure 2C and data not shown). As expected, SMC-*Atg5* deficiency blocked Lc3b lipidation, blocking autophagy and inducing p62 accumulation (Figure 2C) in the aortic media. To study CKD-dependent vascular calcification, CKD was induced by 5/6 nephrectomy. Interestingly, CKD drastically shortened the life span of SMC-specific *Atg5* KO mice (Figure 2D) without affecting levels of serum creatinine, phosphorus, or calcium (Figures S2B–S2D). More importantly, SMC-*Atg5* deficiency

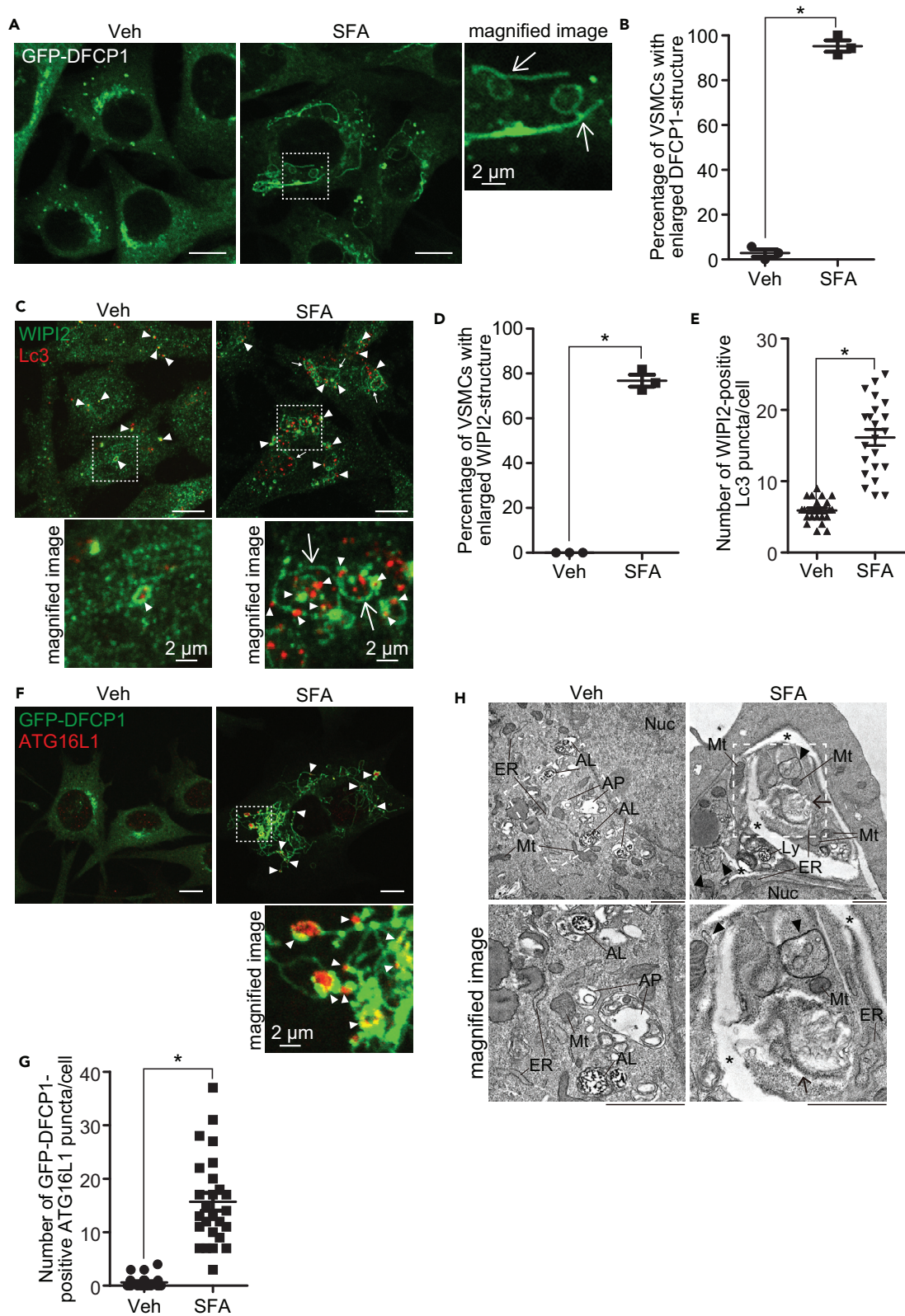


Figure 3. SFAs Lead to Abnormal Formation of DFCP1/WIPI2-Positive Omegasomes and Accumulation of Lc3 in VSMCs

- (A) Confocal microscopy images of GFP-DFCP1 (green) in fixed stable VSMCs expressing GFP-DFCP1 treated with EBSS and BSA (Veh) or 200 μ M C18:0 (SFA) for 2 h. Scale represents 10 μ m. Arrow indicates enlarged tube and ring structure of GFP-DFCP1 with a Ω shape.
- (B) Percentage of VSMCs with one or more enlarged GFP-DFCP1 structures in analysis of Figure 3A. (n = 3, from 35 cells in each experiment; 2-tailed Student's t test). *p < 0.05. Data are represented as mean \pm SEM.
- (C) Confocal microscopy images of endogenous WIPI2 (green) and Lc3 (red) in wild-type VSMCs treated with EBSS and Veh or SFA for 2 h. Scale represents 10 μ m. Arrow indicates enlarged WIPI2 and arrowhead indicates WIPI2-positive Lc3.
- (D) Percentage of VSMCs with enlarged WIPI2 structures (n = 3, from 33 cells in each experiment; 2-tailed Student's t test). *p < 0.05. Data are represented as mean \pm SEM.
- (E) Number of Lc3 punctation with WIPI2 (n = 22, 2-tailed Student's t test). *p < 0.05. Data are represented as mean \pm SEM.
- (F) Confocal microscopy images of GFP-DFCP1 (green) and endogenous ATG16L1 (red) in VSMCs treated with EBSS and Veh or SFA for 2 hr. Scale represents 10 μ m. Arrowhead indicates DFCP1-positive ATG16L1.
- (G) Number of ATG16L1 punctation with GFP-DFCP1 (n = 26, 2-tailed Student's t test). *p < 0.05. Data are represented as mean \pm SEM.
- (H) Electron micrography in wild-type VSMCs treated with EBSS and Veh or SFA for 2 h. Scale represents 1 μ m. Asterisk indicates enlarged membrane structure, arrowhead indicates unclosed membrane as isolation membrane, and arrow indicates Ω -like structure. ER, endoplasmic reticulum; Mt, mitochondria; AP, autophagosome; AL, autolysosome; Nuc, nucleus.

significantly aggravated aortic medial calcification (Figures 2E–2G) and apoptosis (Figures 2H and 2I) and damaged mitochondria accumulation (Figures 2J) 6 weeks after CKD induction.

SFAs Inhibit Starvation-Induced Autophagy at Steps Prior to Degradation in Autolysosomes

Because SFAs inhibit autophagic flux, we put in extensive efforts to elucidate the precise mechanism by which SFAs block autophagy. To enhance the effect of SFAs on autophagy, we performed all of the mechanistic studies under starvation conditions with EBSS treatment. We first performed confocal microscopic analysis with co-immunostaining of Lc3 and Lamp1 to assess whether SFAs affect lysosomal function (Figure S3A). Treatment of VSMCs with SFAs such as C18:0 exhibited significant accumulation of Lc3 compared with vehicle (Figure S3B), but co-localization of Lc3 and Lamp1 was not increased (Figure S3C). Treatment with SCD inhibitor (CAY) also increased total Lc3 but not co-localization of Lc3 and Lamp1, similar to C18:0 treatment. In contrast, treatment with various lysosomal inhibitors such as the protease inhibitors leupeptin, pepstatin A, and bafilomycin A1 increased co-localization of Lc3 and Lamp1 in VSMCs (Figure S3A–S3C). To further evaluate the effect of SFAs on lysosome function and other lysosomal degradation pathways, we examined degradation of EGFR, which can be degraded through the endocytosis-lysosomal pathway in response to EGF (Alwan et al., 2003; Tsuboyama et al., 2016) (Figure S3D). C18:0 did not influence EGF-induced lysosomal EGFR degradation, whereas bafilomycin A1 blocked degradation of EGFR after EGF treatment in VSMCs. These results revealed that SFAs do not affect lysosome function but inhibit autophagy prior to autolysosome formation. We next generated VSMCs stably expressing GFP-Syntaxin 17 (GFP-STX17), a matured autophagosome marker (Itakura et al., 2012; Tsuboyama et al., 2016; Uematsu et al., 2017; Yoshii and Mizushima, 2017), to examine which step of autophagy is affected by SFAs. Based on the immunofluorescence analysis, unlike bafilomycin A1, SFA treatment significantly reduced co-localizations between Lc3 and STX17 (Figures S3E and S3F) and between Lc3 and Lamp1 (Figures S3E and S3G), whereas STX17 and Lamp1 double-negative Lc3 was significantly increased in VSMCs treated with C18:0 (Figures S3E and S3H). These results suggest that SFAs block a step that occurs prior to mature autophagosome formation.

SFAs Induce Abnormal Formation of DFCP1/WIPI2-Positive Omegasomes and Accumulation of Isolation Membranes

We expect that SFAs inhibit autophagy machinery at a step prior to formation of the mature autophagosome. Formation of omegasomes is an early event of autophagosome generation. To determine whether SFAs influence omegasome formation and structures, we generated VSMCs stably expressing GFP-DFCP1 and analyzed them with confocal microscopy (Figure 3A). Because DFCP1 localizes on omegasome structures by binding to PI3P, DFCP1 forms punctate-like structures (Axe et al., 2008). In normal VSMCs (vehicle treatment), DFCP1 formed punctate-like structures in a large proportion (97.1%) and punctates with long tube-like structures in a small proportion (2.9%) (Figures 3A and 3B). Surprisingly, on the other hand, C18:0 treatment induced abnormally enlarged DFCP1 structures that formed large ring shapes similar to the letter Ω and long tube shapes with branches in over 95% of VSMCs, whereas less than 5% showed normal punctate-like structures (Figures 3A and 3B). To confirm that SFAs induce abnormally enlarged omegasome formation, we examined the structures of omegasomes using endogenous WIPI2, another omegasome marker, and analyzed co-localization with Lc3 in VSMCs treated with C18:0 (Figure 3C). WIPI2 formed normal punctate structures in VSMCs treated with vehicle. Similar to DFCP1-positive membranes, C18:0

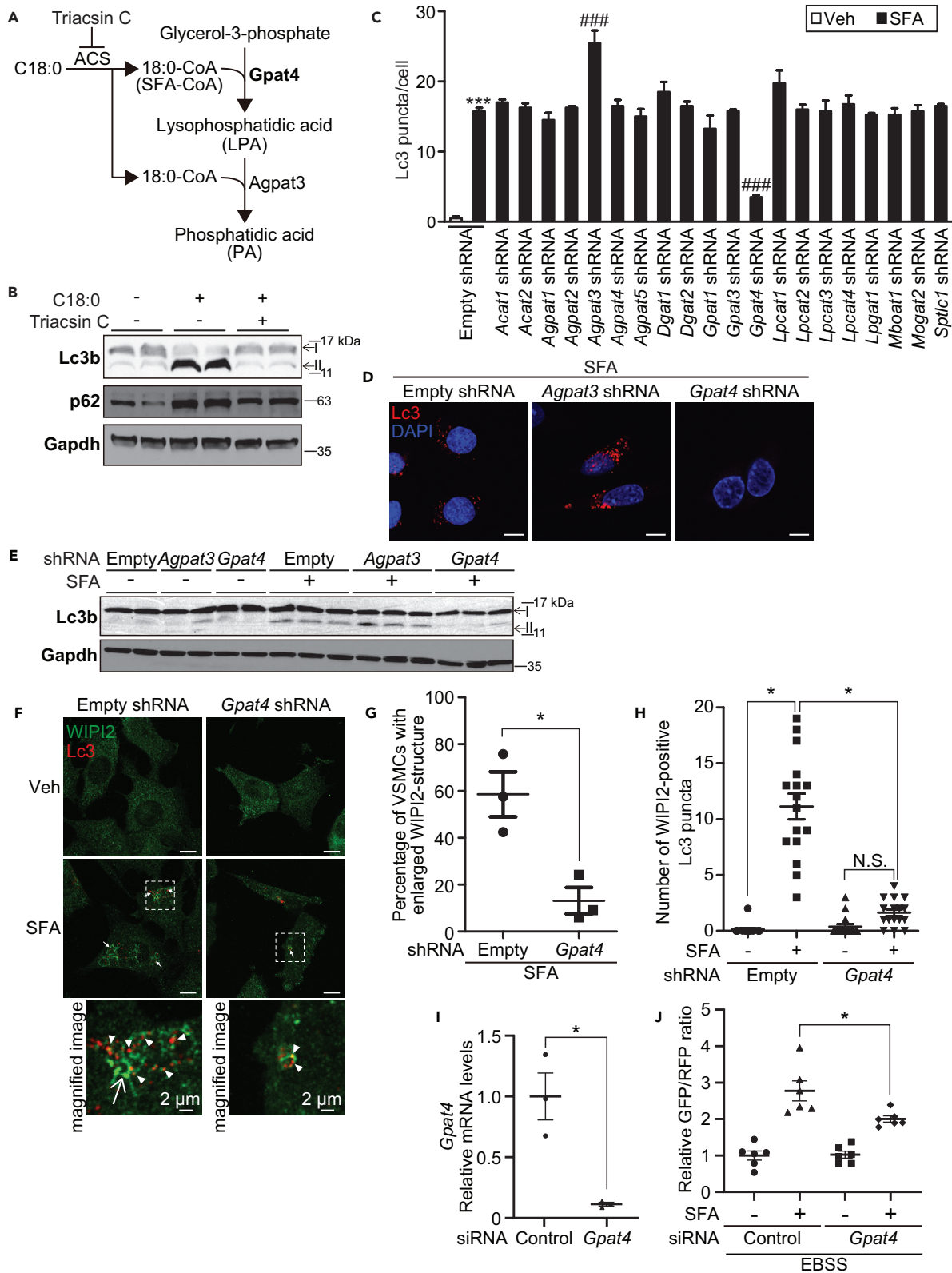


Figure 4. Gpat4 Mediates Accumulation of Lipidated Lc3 and Abnormal Formation of WIPI2-Positive Omeasomes by SFAs

- (A) Scheme of fatty acid metabolism with acyl-CoA synthetase (ACS), Gpat4, and Agpat3. TriacsinC: an acyl-CoA synthetase inhibitor.
- (B) Immunoblot analysis of VSMCs treated with 250 μ M C18:0 with or without 10 μ M Triacsin C for 6 h.
- (C) Number of Lc3 punctations in shRNA-based acyltransferase knockdown (KD) VSMCs treated with BSA (Veh) or 200 μ M C18:0 for 6 h under complete media conditions (n = 4, one-way ANOVA). ***p < 0.001 versus Empty shRNA Veh. ###p < 0.001 versus Empty shRNA SFA. Data are represented as mean \pm SEM.
- (D) Immunofluorescence of Lc3 (red) and DAPI (blue) in empty, Gpat4 and Agpat3 KD VSMCs treated with 200 μ M C18:0 for 6 h under complete media conditions. Scale represents 10 μ m.
- (E) Immunoblot analysis of Gpat4 or Agpat3 KD VSMCs treated with Veh or 250 μ M C18:0 for 6 h under complete media conditions.
- (F) Immunofluorescence of endogenous WIPI2 (green) and Lc3 (red) in empty and Gpat4 KD VSMCs treated with Veh or 200 μ M C18:0 for 2 h under complete media conditions. Arrow indicates enlarged WIPI2 and arrowhead indicates WIPI2-positive Lc3 punctation. Scale represents 10 μ m.
- (G) Percentage of VSMCs with enlarged WIPI2 structures (n = 3, from 33 cells in each experiment; 2-tailed Student's t test). *p < 0.05. Data are represented as mean \pm SEM.
- (H) Number of Lc3 punctation with WIPI2 from Figure 4F analysis (n = 15, one-way ANOVA). *p < 0.05; N.S., not significant. Data are represented as mean \pm SEM.
- (I) Levels of Gpat4 mRNA by qRT-PCR in 50 nM negative control or Gpat4 siRNA-transfected VSMCs. (n = 3, 2-tailed Student's t test). *p < 0.05. Data are represented as mean \pm SEM.
- (J) Measurement of autophagic flux with Gpat4 knockdown. Stable VSMCs expressing GFP-LC3-RFP-LC3 Δ G were transfected with 50 nM negative control or Gpat4 siRNA. After 24 h, VSMCs were co-treated with Veh or 500 μ M C18:0 under starvation conditions for 6 h. GFP/RFP ratio data was expressed as fold value against Veh (n = 6, one-way ANOVA). *p < 0.05.

treatment drastically induced abnormal enlargement of WIPI2-positive omeasomes (Figures 3C and 3D). In addition, Lc3 was more significantly accumulated on WIPI2-positive membranes in VSMCs treated with C18:0 than VSMCs treated with vehicle (Figures 3C and 3E), suggesting accumulation of unclosed immature autophagosomes (isolation membranes) in the omeasomes. To confirm the accumulation of isolation membranes, we used ATG16L1 as an isolation membrane-specific marker. VSMCs treated with C18:0 had significantly higher DFCP1-positive ATG16L1 punctates (Figures 3F and 3G). Consistent with detailed confocal immunofluorescence analyses, electron microscopy analysis revealed that accumulation of abnormal enlarged membrane structures and isolation membranes was specifically observed in VSMCs treated with C18:0 (Figure 3H). We next examined whether the modulations of PI3 kinase- (Vps34) and PI3P phosphatase- (myotubularin-related phosphatase, Mtmr) mediated PI3P homeostasis contribute to SFA-induced omeasome formation. The total amount of PI3P was not changed in C18:0-treated VSMCs (Figure S4A). Abnormal omeasome formation by C18:0 treatment was significantly attenuated by the inhibition of a PI3 kinase, VPS34 (Figures S4B and S4C). In addition, unlike C18:0 treatment, the modulation of PI3P by the overexpression of VPS34-FLAG or the knockdown of Mtmr did not induce abnormal DFCP1-positive omeasome formation in VSMCs (Figures S4D, S4E, and Table S1). Two studies consistently reported that autophagy-related Mtmr-6, -8, and -9 did not induce abnormal omeasome formation (Mochizuki et al., 2013; Zou et al., 2012). These data suggest that modulations of Vps34 and Mtmr-regulated PI3P did not contribute to SFA-induced abnormal omeasome formation. SFA-induced abnormal omeasome formation and accumulation of isolation membranes occurred not only in VSMCs but also in HeLa cells (Figures S4F–S4H). These data suggest that SFAs lead to abnormal formation of omeasomes, resulting in accumulation of Lc3-II-anchored isolation membranes, which is a common effect of SFAs.

Characterization of SFA-Induced Abnormal Formation of Omeasomes

To examine how SFAs induce the abnormal formation of omeasomes, we captured a live image of VSMCs expressing GFP-DFCP after SFA treatment. As shown in Video S1, the peak of SFA-induced abnormal formation of omeasomes occurred between 0.5 and 1 h after C18:0 treatment. Five major characteristics of abnormal omeasome formation were detected (Video S1 and Figure S4): (1) enlargement: a single omeasome is simply enlarged (Figure S4I); (2) multiplication: an original omeasome produces another omeasome, which produces another omeasome (Figure S4J); (3) elongation: the omeasome membrane is simply elongated (Figure S4K); (4) clusterization: multiple omeasomes approach each other and form a cluster (Figure S4L); (5) fusion: some of the omeasome clusters fuse and generate a single large omeasome (Figure S4M). These abnormal omeasome formations were not observed in VSMCs treated with vehicle (Video S2).

Gpat4 Mediates Accumulation of Lc3 and Enlargement of WIPI2-Positive Omeasomes through SFA Treatment

To examine whether free SFAs or SFA-derived metabolites affect autophagy, we first modified acyl-CoA synthetase (ACS) with Triacsin C, an inhibitor of ACS. Triacsin C treatment completely blocked the incorporation of fatty acids into acyl lipids (Figure 4A). In the presence of Triacsin C, C18:0 treatment no longer

increased levels of autophagic substrates such as Lc3b-II and p62 (Figure 4B). These data suggest that SFAs must be incorporated into an acyl-lipid to inhibit autophagic flux. We therefore next examined which acyltransferase contributes to SFA-mediated autophagy inhibition using an shRNA-mediated acyltransferase knockdown (KD) VSMC library that we previously generated (Masuda et al., 2015) (Figure 4C). Each acyltransferase KD VSMC was treated with C18:0 for 2 h. Similar to Figures 1F and 1G, C18:0 treatment significantly induced accumulation of Lc3 puncta compared with vehicle. Interestingly, *Gpat4* and *Agpat3* KD reciprocally regulated SFA-induced accumulation of Lc3 in VSMCs (Figures 4C and 4D). *Gpat4* KD reduced SFA-induced Lc3 puncta accumulation by 79%, whereas *Agpat3* knockdown significantly increased the number of Lc3 puncta in the presence of SFAs. In addition, immunoblot analysis confirmed that *Gpat4* KD reduced levels of Lc3b-II increased with C18:0 treatment, whereas *Agpat3* KD increased levels (Figure 4E). We next examined whether *Gpat4* contributes to SFA-induced abnormal enlargement of WIPI2-positive omegasomes and accumulation of isolation membranes. *Gpat4* KD reduced levels of abnormally enlarged WIPI2 membranes and accumulation of Lc3 on WIPI2-positive omegasomes under SFA treatment, suggesting that *Gpat4* mediates SFA-induced abnormal enlargement of omegasomes, leading to accumulation of Lc3-positive isolation membranes (Figures 4F–4H). To analyze the effect of *Gpat4* knockdown on SFA-induced autophagic flux inhibition, stable VSMCs expressing GFP-LC3-RFP-LC3ΔG probe were transfected with *Gpat4* siRNA and then treated with SFAs under starvation conditions. *Gpat4* siRNA treatment significantly reduced levels of *Gpat4* in VSMCs by 88% (Figure 4I). *Gpat4* knockdown significantly attenuated autophagic flux inhibition by C18:0 compared with scrambled siRNA (Figure 4J).

Saturated LPAs Induce Autophagic Flux by Inducing Abnormal Formation of DFCP1-Positive Omegasomes

Gpat4 and *Agpat3* catalyze the initial two steps of glycerolipid synthesis (Fagone and Jackowski, 2009). *Gpat4* is the first enzyme to catalyze the conversion of glycerol-3-phosphate to 1-acyl-lysophosphatidic acid (LPA), which is further acylated by *Agpat3* to generate phosphatidic acid (PA) (Figure 4A). Our previous lipidomic study revealed that abnormally excessive amounts of fully saturated LPAs (i.e. 18:0-LPA) in addition to fully saturated PAs (i.e. 18:0/18:0-PA) were accumulated in the aortic medias of SMC-*Scd1/2* KO mice and cultured VSMCs treated with SFAs (Masuda et al., 2015). We therefore hypothesized that accumulation of saturated LPAs, LPAs derived from SFAs, mediate inhibition of autophagic flux. To confirm our hypothesis, we treated VSMCs with an SFA (C18:0), saturated and unsaturated LPAs (18:0-LPA and 18:1-LPA), and fully saturated and fully unsaturated PAs (18:0/18:0-PA and 18:1/18:1-PA). The immunoblot analysis with Lc3b-II shows that 18:0-LPA but not 18:1-LPA dose-dependently induced accumulation of Lc3b-II (Figure 5A). However, treatment with 18:0-LPA was unable to activate ER stress signals such as ATF4, CHOP, and BiP (Figure 5B). Unlike C18:0 and 18:0-LPA, both 18:0/18:0-PA and 18:1/18:1-PA did not induce accumulation of Lc3b-II (Figure 5C). In addition, treatment with 18:0/18:0-PA did not affect total amounts of 18:0-LPA in VSMCs (Figure 5D). To confirm that 18:0-LPA inhibits autophagic flux similar to SFAs, VSMCs expressing GFP-LC3-RFP-LC3ΔG probe were treated with 18:0-LPA. 18:0-LPA treatment significantly increased the ratio of GFP/RFP fluorescence, indicating that 18:0-LPA inhibits autophagic flux (Figure 5E). To evaluate whether 18:0-LPA modulates DFCP1-positive membrane structures, we performed confocal microscopy analysis with stable GFP-DFCP1 VSMCs treated with 18:0-LPA and 18:0/18:0-PA (Figures 5F and 5G). DFCP1 formed enlarged structures under 18:0-LPA treatment, similar to C18:0 treatment, whereas 18:0/18:0-PA did not induce enlargement of DFCP1-positive membrane structures. Electron microscopy analysis confirmed abnormally enlarged membrane structures in VSMCs treated with 18:0-LPA but not in VSMCs treated with vehicle (Figure 5H).

SFAs Accumulate as Saturated LPAs in the Contact Sites between DFCP1-Positive Omegasomes and Mitochondria-Associated Membranes

To determine which organelle is responsible for abnormal formation of omegasomes by SFAs, we performed immunostaining of various organelle markers in GFP-DFCP1 cells (Figures S5A and S5B). Normally, DFCP1 co-localizes with a golgi marker, RCAS1, at the close region of the nucleus (Figure S5A). Although enlarged DFCP1-positive omegasomes in VSMCs treated with C18:0 do not localize with either RCAS1, a lysosomal marker Lamp1, or lipid droplets stained with LipidTox Red (Figures S5A and S5B), they are located in the close vicinity of an ER marker, Calnexin, and a mitochondria marker, Tomm20 (Figure S5A, magnified images). In addition, abnormally enlarged DFCP1 was localized next to other ER markers, KDEL and Tomm20, suggesting that abnormally enlarged omegasomes are possibly associated with contact sites between the ER and mitochondria (Figure S5C). The contact sites between ER-mitochondria and DFCP1 were significantly increased in VSMCs treated with C18:0 (Figures S5C and S5D). Moreover, electron

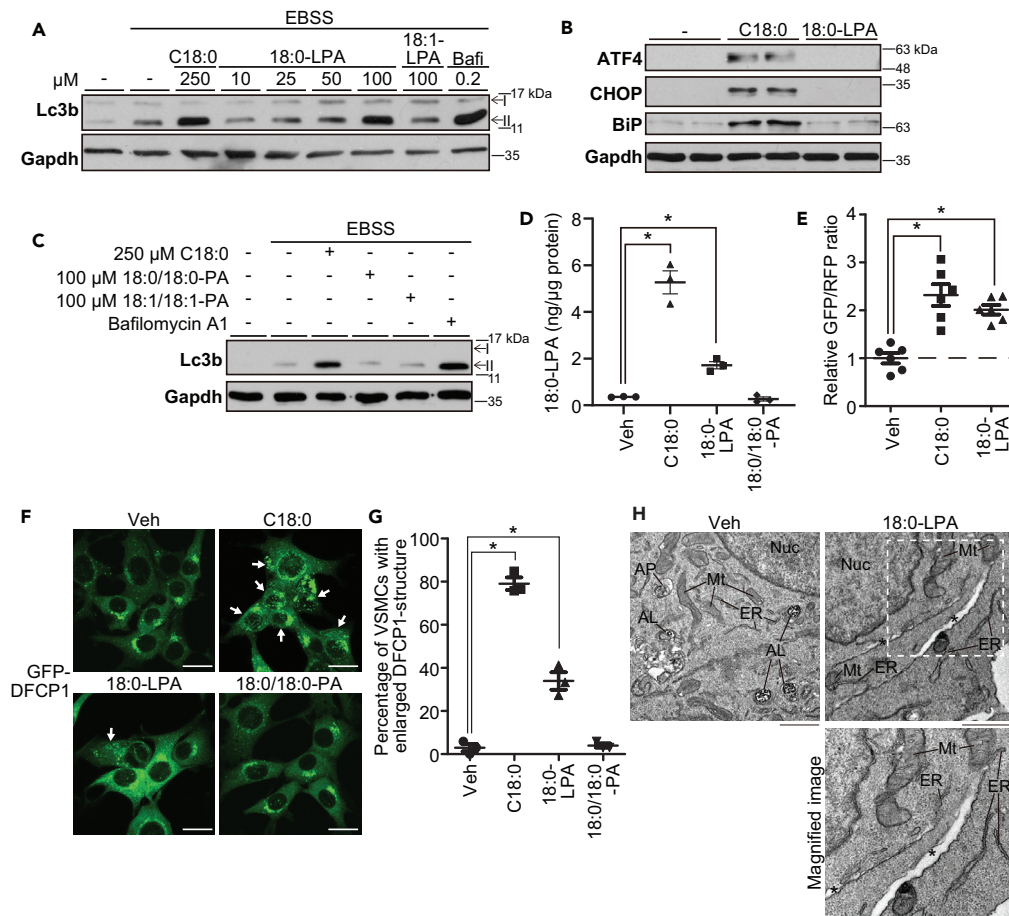


Figure 5. Saturated LPAs, but Not Fully Saturated PAs, Induce Accumulation of Lipidated Lc3b-II and Abnormal Enlargement of DFCP1-Positive Omegasomes in VSMCs

(A) Immunoblot analysis of VSMCs treated with BSA (–), C18:0, 18:0-LPA, 18:1-LPA, or bafilomycin A1 under EBSS conditions for 2 h.

(B) Immunoblot analysis of ER stress proteins in VSMCs treated with BSA (–), C18:0, or 18:0-LPA under complete media conditions for 6 h.

(C) Immunoblot analysis of VSMCs treated with BSA (–), C18:0, 18:0/18:0-PA, 18:1/18:1-PA, or bafilomycin A1 under EBSS conditions for 2 h.

(D) LC-MS-based absolute levels of 18:0-LPA species of VSMCs after 6 h of treatment with 300 μ M C18:0, 100 μ M 18:0-LPA, or 100 μ M 18:0/18:0-PA (n = 3, one-way ANOVA). *p < 0.05. Data are represented as mean \pm SEM.

(E) Measurement of autophagic flux using stable VSMCs expressing GFP-LC3-RFP-LC3 Δ G treated with BSA (Veh), 300 μ M C18:0, 100 μ M 18:0-LPA, or 200 nM bafilomycin A1 under EBSS conditions for 6 h. GFP/RFP ratio data were expressed as fold value against vehicle (n = 6, one-way ANOVA). *p < 0.05.

(F) Confocal microscopy images in stable VSMCs expressing GFP-DFCP1 treated with EBSS and Veh, 200 μ M C18:0, 100 μ M 18:0-LPA, or 100 μ M 18:0/18:0-PA for 2 h. Scale represents 20 μ m and arrow indicates VSMCs with enlarged GFP-DFCP1 structures.

(G) Percentage of VSMCs with enlarged GFP-DFCP1 structures in Figure 5F analysis (n = 3, from 33–34 cells in each experiment, one-way ANOVA). *p < 0.05. Data are represented as mean \pm SEM.

(H) Electron micrograph of wild-type VSMCs co-treated with 100 μ M 18:0-LPA and EBSS for 2 h. Scale represents 1 μ m. Asterisk indicates enlarged membrane structure. ER, endoplasmic reticulum; Mt, mitochondria; Nuc, nucleus.

micrographs of SFA-treated VSMCs showed that most of the enlarged membrane structures were connected to the contact sites of the ER and mitochondria (Figure 6A). ER membranes and mitochondria membranes form mitochondria-associated membranes (MAMs), which play many physiological roles such as autophagosome formation with the Beclin-1-Vps34 complex (Hamasaki et al., 2013). In addition, the MAM is a major site of glycerolipid synthesis (Man et al., 2006; Vance, 1990). DFCP1 proteins are translocated to the MAM under starvation (Hamasaki et al., 2013). To determine tight associations between abnormally

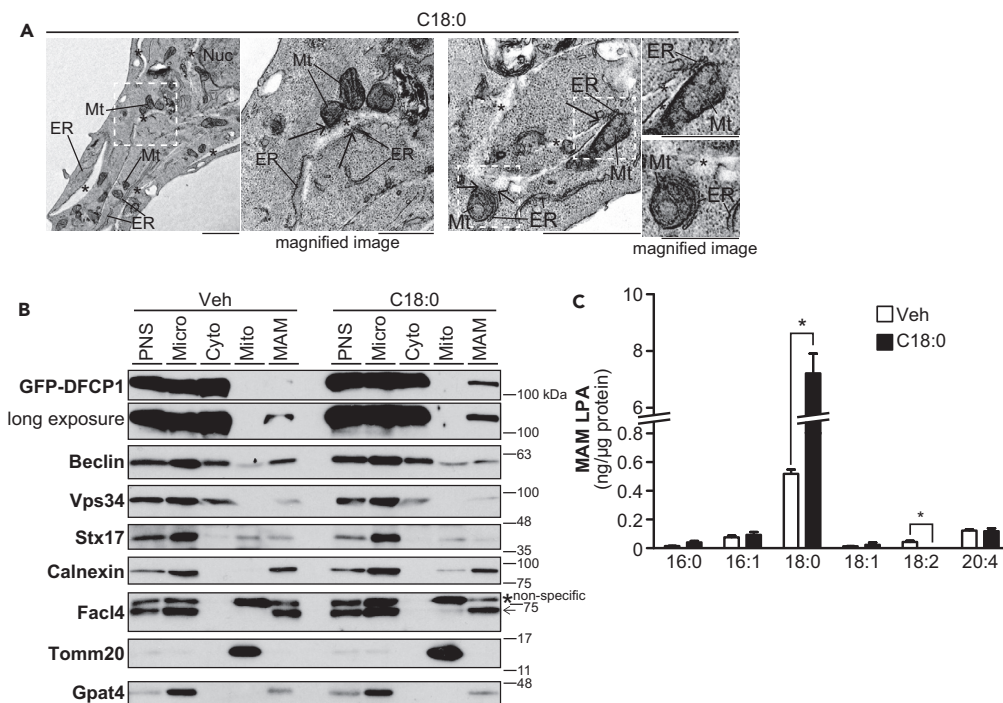


Figure 6. SFAs Lead to Accumulation of Saturated LPAs on Mitochondria-Associated Membrane (MAM) Contact Sites with DFCP1-Positive Omegasomes in VSMCs

(A) Electron micrograph of wild-type VSMCs co-treated with 200 μ M C18:0 and EBSS for 2 h. Scale represents 1 μ m or 500 nm in the magnified image. Asterisk indicates enlarged membrane structure and arrow indicates connections between enlarged membrane and ER, mitochondria, or ER-mitochondria contact site. ER, endoplasmic reticulum; Mt, mitochondria; Nuc, nucleus.

(B) Immunoblot analysis of post nuclear supernatant (PNS), microsome (Micro), cytosol (Cyto), mitochondria (Mito), and MAM fractions of stable VSMCs expressing GFP-DFCP1 co-treated with EBSS and BSA (Veh) or C18:0 (SFA) for 2 h.

(C) LC-MS-based absolute levels of LPA species of purified MAM fractions ($n = 3$, 2-tailed Student's t test). * $p < 0.05$. Data are represented as mean \pm SEM.

enlarged DFCP1-positive omegasomes and the MAM, we prepared MAM fractions from vehicle- and SFA-treated VSMCs (Figure 6B). The immunoblot analysis shows that MAM fractions from both vehicle- and SFA-treated VSMCs expectedly contain MAM markers such as Calnexin and FacI4 proteins. Furthermore, PI3K complexes such as Beclin and Vps34 were present in MAM fractions. In the MAM of SFA-treated VSMCs, levels of DFCP1 protein were increased compared with those from vehicle-treated VSMCs (Figure 6B), consistent with the confocal analysis shown in Figures S5C and S5D. Next, we profiled the amount of lysophosphatidic acid species in MAM fractions using an LC/MS-based measurement (Figure 6C). Levels of 18:0-LPA were significantly increased by 14-fold in the MAM from VSMCs treated with C18:0 compared with vehicle. Because MAM fractions from VSMCs treated with C18:0 contain significant amounts of DFCP1, the elevation of 18:0-LPA could be associated with abnormally enlarged DFCP1-membranes. Therefore, we next performed OptiPrep-fractionation to isolate DFCP1-positive membranes (Figures S6A and S6B). Immunoblot analysis showed that GFP-DFCP1 protein was mainly detected on fractions 11, 12, 13, and 14 in both vehicle- and SFA-treated VSMCs (Figure S6A). Because only fraction 11 of SFA-treated VSMCs contains Lc3b-II, Tomm20, and Calnexin proteins, we used fraction 11 as a DFCP1-enriched membrane fraction. LC/MS analysis showed that levels of 18:0-LPA increased by 6-fold in DFCP1-enriched membranes from VSMCs treated with C18:0 (Figure S6B). Interestingly, endogenous Gpat4 protein was detected in MAM fractions from both control and C18:0-treated VSMCs (Figure 6B). To examine whether Gpat4 localizes in the contact site of the MAM and DFCP1 membranes to generate 18:0-LPA as a source of membrane lipids, we analyzed VSMCs overexpressing GFP-DFCP1 and GPAT4-tdTomato by confocal microscopy. As shown in Figures 7A and 7B, SFA treatment showed an increased number of GPAT4 close to the double-positive sites of Tomm20 and DFCP1. In addition, over 85% of Lc3 puncta are observed in proximity with GPAT4 in VSMCs (Figures S6C–S6E). These data suggest that Gpat4 might localize at the MAM and autophagosome formation sites and maybe one of the enzymes indirectly providing lipids for omegasome

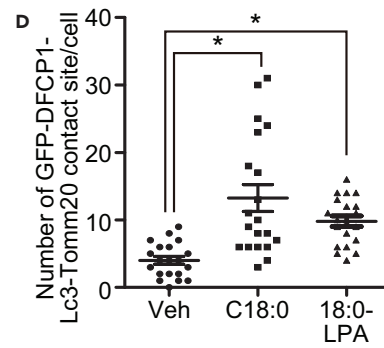
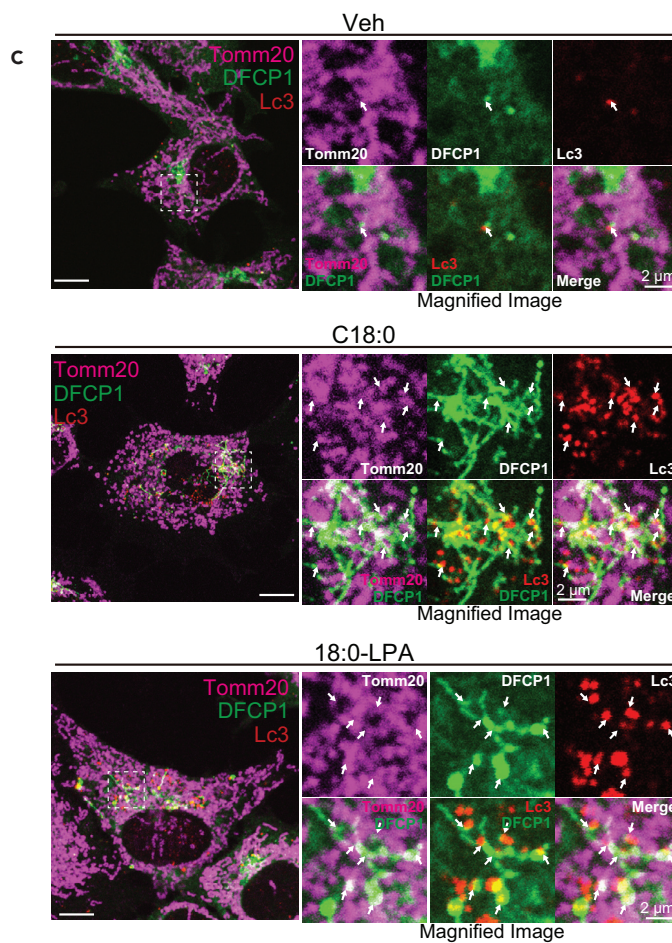
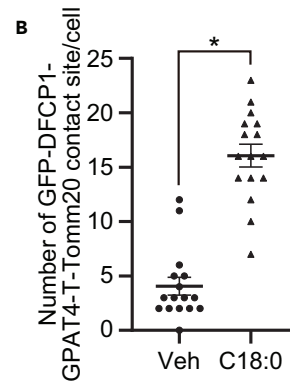
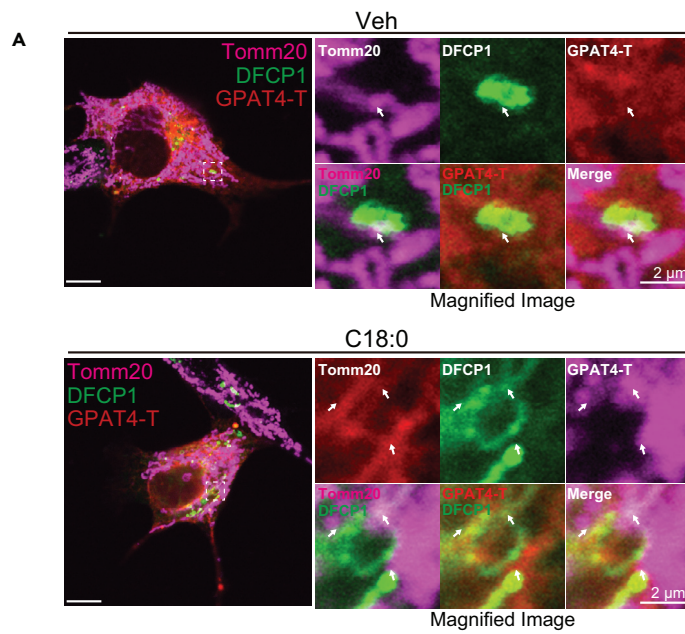


Figure 7. SFAs Increase GPAT4 Localized in Close Proximity to the Double-Positive Site of Tomm20 and DFCP1 Omegasome in VSMCs

(A) Confocal microscopy images of Tomm20 (magenta), GFP-DFCP1 (green), or GPAT4-tdTomato (GPAT4-T) (red) in VSMCs stably expressing GFP-DFCP1 and GPAT4-tdTomato treated with Veh or SFA under EBSS conditions for 2 h. Scale represents 10 μ m. Arrow indicates Tomm20, GFP-DFCP1, and GPAT4-tdTomato contact sites.

(B) Number of GFP-DFCP1-GPAT4-Tomm20 contact sites (n = 16, 2-tailed Student's t test). *p < 0.05. Data are represented as mean \pm SEM.

(C) Confocal microscopy images of Tomm20 (magenta), GFP-DFCP1 (green), and Lc3 (red) in stable VSMCs expressing GFP-DFCP1 co-treated with Veh, C18:0, or 18:0-LPA under EBSS conditions for 2 h. Scale represents 10 μ m. Arrow indicates Tomm20, DFCP1, and Lc3-contact site.

(D) Number of GFP-DFCP1-Lc3-Tomm20 contact sites in Figure 7C (n = 20, One-way ANOVA). *p < 0.05. Data are represented as mean \pm SEM.

formation and enlargement. To confirm that DFCP1-omegasomes associated with the MAM are the site of isolation membrane formation and accumulation in VSMCs treated with C18:0 and 18:0-LPA, we performed immunofluorescence analysis to analyze the co-localization of GFP-DFCP1 with Lc3 and Tomm20 (Figures 7C and 7D). Lc3 puncta were more accumulated on the DFCP1 membrane next to Tomm20-positive signals in C18:0- and 18:0-LPA-treated VSMCs than in vehicle-treated VSMCs.

Unsaturated LPAs Block SFA-Induced Abnormal Enlargement of DFCP1-Positive Omegasomes, Accumulation of Lipidated Lc3, and Calcification in VSMCs

UFAs attenuate SFA-induced lipotoxicity (Listenberger et al., 2003; Masuda et al., 2012, 2015). We examined whether co-treatment of unsaturated LPA (18:1-LPA) blocks SFA-induced abnormal formation of GFP-DFCP1 structures using confocal microscopy (Figures S7A and S7B). UFAs (C18:1) significantly blocked SFA-induced enlargement of DFCP1 membranes. Co-treatment with 18:1-LPA also reduced SFA-induced abnormally enlarged GFP-DFCP1 structures (Figures S7A and S7B). In contrast, fully unsaturated PAs (18:1/18:1-PA) did not influence SFA-induced enlargement of GFP-DFCP1 omegasomes. In the immunoblot analysis, C18:1 inhibited SFA-induced accumulation of Lc3b-II (Figure S7C). Similarly, 18:1-LPA also dose-dependently inhibited C18:0-induced Lc3b-II accumulation (Figure S7D). LPA is a signaling metabolite that works through lysophosphatidic acid receptors (LPARs) in plasma membranes. To study whether the effect of 18:1-LPA occurs via LPARs, VSMCs were treated with LPAR inhibitors such as Brp-LPA, AM095, and H2L5186303 in the presence of 18:1-LPA and C18:0. However, none of the LPAR inhibitors affected the effects of C18:0 and LPA on autophagy (Figure S7E). These results suggest that effects of SFAs and LPAs on the modulation of Lc3b-II are not dependent on LPA receptor signaling.

Gpat4-Generated Saturated LPAs Elicit Lipotoxic Effects In Vitro and In Vivo

We next examined whether 18:0-LPA mediates SFA-induced lipotoxicities such as VSMC mineralization and apoptosis. Similar to C18:0, 18:0-LPA significantly increased levels of matrix calcium in VSMCs, whereas supplementation with 18:1-LPA, similar to C18:1, reduced mineralization (Figures 8A–8D) and levels of the cleavage (active) form of caspase 3 induced by C18:0 treatment (Figure 8E). To study SFA-mediated lipotoxicity through Gpat4-mediated saturated LPA production *in vivo*, we crossed SMC-Scd1/2 KO mice with Gpat4 KO mice to generate SMC-Scd1/2 KO; Gpat4 triple KO mice. Consistent with our previous report (Masuda et al., 2015), SMC-Scd1/2KO mice developed severe aortic medial calcification, vascular apoptosis, and accumulation of autophagic substrates such as p62 and Fam134b2, accompanied by significantly increased levels of saturated LPAs such as 16:0-LPA and 18:0-LPA (Figures 8F–8J). More importantly, Gpat4 deficiency completely blocked SCD deficiency-induced vascular calcification, apoptosis, and inhibition of autophagy (Figures 8F–8J). In addition, Gpat4 deficiency completely blocked accumulation of aortic saturated LPAs by SMC-SCD deficiency (Figure 8J).

DISCUSSION

SFA-induced lipotoxicity is mediated by modifications of various pathways including apoptosis, ER stress, autophagy, oxidative stress, cell cycle inflammation, and membrane dynamics (Anderson et al., 2012; Brodeur et al., 2013; Holthuis and Menon, 2014; Hsiao et al., 2014; Listenberger et al., 2003; Masuda et al., 2012, 2015; Mei et al., 2011; Park et al., 2019; Wen et al., 2011). We previously showed that inhibition of SCD induces aortic medial calcification by accumulating SFA-derived metabolites in VSMCs (Masuda et al., 2015). In addition, CKD increases circulating SFAs in humans (Masuda et al., 2015). These results suggest that SFA-induced lipotoxicity is a major cause of vascular calcification in CKD. However, which lipotoxic pathway is responsible for the development of vascular calcification is not completely understood. The autophagy-lysosomal degradation pathway is a protective mechanism in various organs against diseases such as neurodegenerative diseases, liver diseases, muscular disorders, and pathogen infections (Dikic and Elazar, 2018; Leidal et al., 2018; Maiuri and Kroemer, 2019; Ren and Zhang, 2018). In this study we showed direct

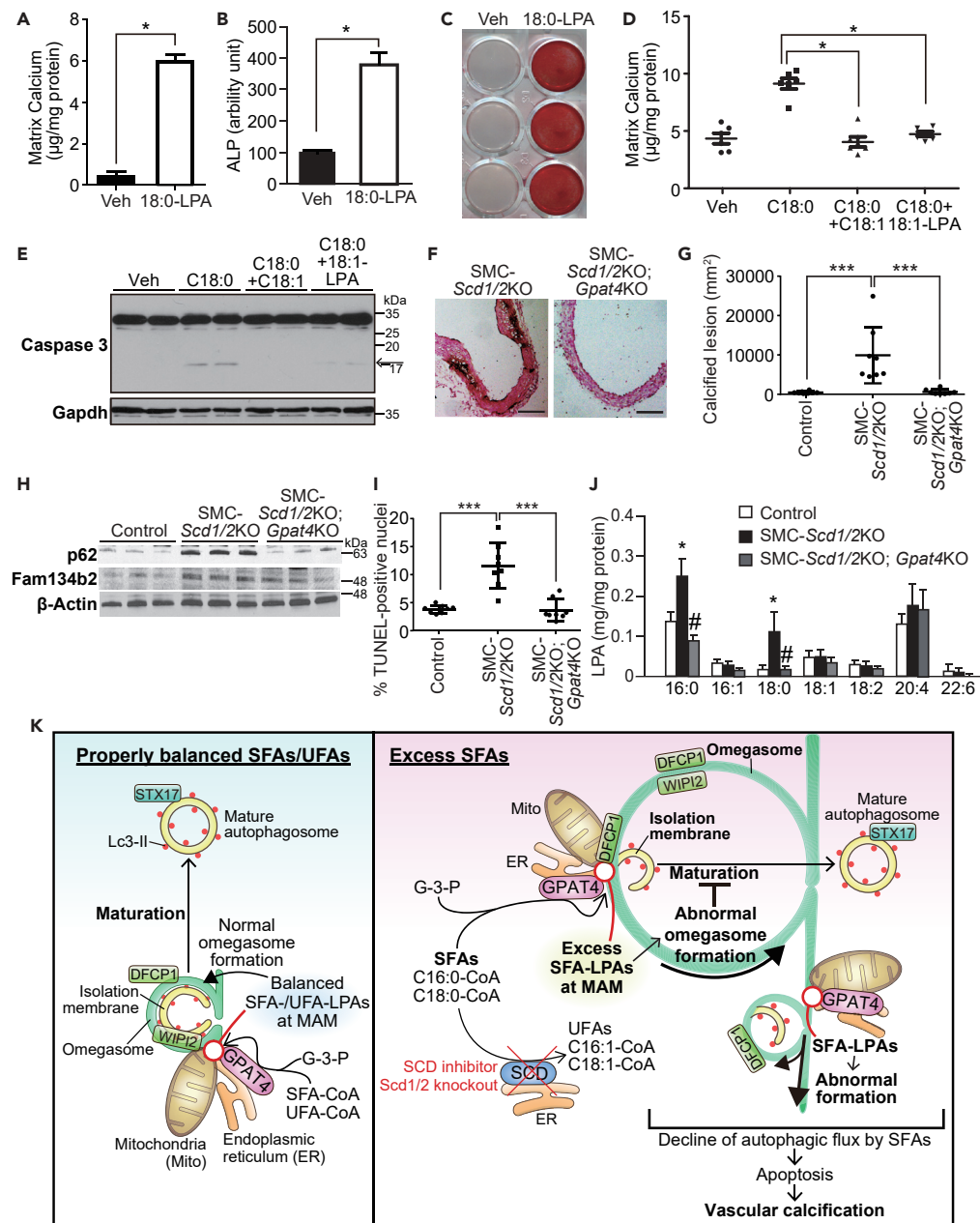


Figure 8. *Gpat4* Knockout Blocked Vascular Calcification in *Scd1/2* Knockout Mice After 5/6 Nephrectomy
 (A and B) (A) Mineralization and (B) ALP activity of VSMCs co-treated with 2.6 mM Pi and Veh or 18:0-LPA every 2 days for 6 days ($n = 6$, 2-tailed Student's *t* test). * $p < 0.05$. Data are represented as mean \pm SEM.
 (C) Alizarin red staining of VSMCs co-treated with Pi and Veh or 18:0-LPA for 6 days.
 (D) Mineralization of VSMCs co-treated with 2.6 mM Pi and 200 μM C18:0 and BSA, 200 μM C18:1, or 20 μM 18:1-LPA every 2 days for 6 days ($n = 6$, one-way ANOVA). * $p < 0.05$. Data are represented as mean \pm SEM.
 (E) Immunoblot analysis of caspase 3 and Gapdh in VSMCs treated with 200 μM C18:0 and BSA, 200 μM C18:1, or 20 μM 18:1-LPA for 16 h. Arrow indicates cleaved (active) form of Caspase-3.
 (F) Photograph ($\times 10$ magnification) of the lesions in aortic arches with von Kossa staining in SMC-*Scd1/2* KO mice and SMC-*Scd1/2* and *Gpat4* triple KO mice. Scale represents 200 μm .
 (G) Quantitative analysis of calcified lesions in Figure 8F analysis ($n = 8$, one-way ANOVA). $p < 0.001$. Data are represented as mean \pm SEM.
 (H) Levels of autophagy-specific substrates in the aortic medias of SMC-*Scd1/2* KO; *Gpat4* KO mice.

Figure 8. Continued

(I and J) (I) Percentage of aortic media apoptosis and (J) levels of LPA in the aortic medias of SMC-*Scd1/2* KO; *Gpat4* KO mice (n = 8, One-way ANOVA). *p < 0.05 versus control, #p < 0.05 versus SMC-*Scd1/2* KO, and *p < 0.001. Data are represented as mean ± SEM.

(K) A model of SFA-induced vascular calcification through impairment of autophagosome maturation. Excess SFAs created through SCD inhibition and SFA supplementation are converted to saturated LPAs by GPAT4 at the MAM. Accumulation of saturated LPAs in MAM-associated omegasomes disrupts the proper balance of SFA-LPAs and UFA-LPAs, which causes abnormal formation of omegasomes, and excess production and accumulation of Lc3-II-positive isolation membranes, resulting in the inhibition of autophagic flux. Saturated LPA-mediated autophagy inhibition induces vascular apoptosis and calcification. G-3-P; glycerol-3-phosphate, LPA; lysophosphatidic acid.

evidence that autophagy in VSMCs plays a protective role in the pathogenesis of vascular calcification in CKD. CKD and SCD deficiency induced significant accumulation of aortic proteins (Lc3b-II, p62 and Fam134b2) specifically degraded through autophagy. More strikingly, SMC-specific Atg5 deficiency, and therefore inhibition of VSMC autophagy, strongly induces vascular calcification and apoptosis, resulting in significant increases in mortality of CKD mice. These results demonstrate that SFA-mediated autophagy inhibition plays a causative role in vascular calcification.

Due to the lack of detailed autophagic flux and mechanistic studies, the effect of SFAs and SCD on autophagy regulation is controversial (Khan et al., 2012; Liu et al., 2015; Tan et al., 2012, 2014). Most of the conclusions in the previous studies were made based on the results of immunoblot analysis and/or confocal microscopic analysis with LC3B. We therefore made extensive efforts to elucidate the effect of SFAs on autophagic flux and the precise mechanism by which SFAs modulate autophagy machinery. Although VSMCs were mainly used in this study, the mechanisms underlying the modulation of autophagy by SFAs are very similar in any cell type as SFAs also elicit the inhibitory effect of autophagy in two other common cell lines, HeLa and NIH-3T3. In this study, we conclude that SFAs such as C18:0 and C16:0 and the inhibition of SCD both inhibit autophagic flux based on the study using the GFP-LC3-RFP-LC3ΔG probe that enabled us to most accurately analyze it (Kaizuka et al., 2016; Yoshii and Mizushima, 2017). We therefore conclude that the accumulation of Lc3b-II and p62 in cells treated with SFAs and in the aortic media of SMC-*Scd1/2* KO mice is due to SFA-induced autophagy inhibition. More importantly, in this study we have elucidated the precise mechanism by which SFAs mediate the inhibition of autophagy and demonstrate that SFA accumulation induces abnormal enlargement of MAM-originated omegasomes, which leads to accumulation of Lc3b-II positive isolation membranes on omegasomes.

We previously reported that GPAT4 is one of the enzymes in SFA-induced lipotoxicity and vascular calcification (Masuda et al., 2015), which has also been shown by two recent studies (Piccolis et al., 2019; Zhu et al., 2019). In addition, we identified that fully saturated PAs produced by the GPAT4-AGPAT3/5 reaction mediate SFA-induced ER stress. However, which SFA metabolite mediates the inhibitory effect of SFAs in autophagy has not been studied. Although SFA-induced ER stress was blocked by the inhibition of three enzymes, *Gpat4*, *Agpat3*, and *Agpat5* (Masuda et al., 2015), SFA-induced autophagy inhibition was inhibited only by *Gpat4* inhibition. Interestingly, *Agpat3* blockage augments SFA-induced Lc3b accumulation. SFA treatment drastically induces accumulation of saturated LPAs (Masuda et al., 2015). Treatment with exogenous 18:0-LPA, a saturated LPA, but not fully saturated PAs such as 18:0/18:0-PA, replicates SFA-induced autophagy inhibition including the inhibition of autophagic flux and the generation of abnormally enlarged omegasomes, suggesting that saturated LPAs are specific SFA metabolites that affect omegasome formation and autophagic flux under excess SFAs. Furthermore, co-treatment with unsaturated LPAs such as 18:1-LPA, but not unsaturated PAs such as 18:1/18:1-PA, attenuates SFA-induced autophagy inhibition. These data demonstrate that *Gpat4* converts SFAs to saturated LPAs, disrupting the proper balance of SFA-LPAs and UFA-LPAs (ie, 18:0-LPA/18:1-LPA), causing abnormal enlargement of omegasomes. LPAs containing UFAs are a termination factor for the enlargement of omegasomes. Another interesting finding in this study is that *Gpat4* is located in the contact sites between abnormally enlarged omegasomes and the MAM, which are increased by SFAs. The sources of isolation membranes have not been fully defined yet, but they possibly come from the ER, mitochondria, and Golgi, recycling endosomes and the plasma membrane through Atg9-mediated vesicle transport (Hailey et al., 2010; Lamb et al., 2013; Mari et al., 2010; Ohashi and Munro, 2010; Puri et al., 2013; Ravikumar et al., 2010; Yamamoto et al., 2012). In addition, the ER-mitochondria contact site (the MAM) is a major site of autophagosome production (Hamasaki et al., 2013). Furthermore over 85% of autophagosome generation sites (Lc3 positive) are closely co-localized with GPAT4 in the cells

treated with C18:0 (Figures S6C–S6E). The ER, mitochondria, and contact sites could directly supply lipids to omegasomes and isolation membranes. In fact, SFA treatment induces accumulation of saturated LPAs in the MAM and DFPC1-enriched membranes. The source of omegasome membrane lipids is also not clear, but our data suggest that glycerophospholipids such as LPAs synthesized on the MAM are also used as a major omegasome lipid source under excess SFAs. Gpat4 on the MAM supplies saturated LPAs, which causes the abnormal enlargement of omegasomes. In addition, exogenous 18:0-LPA induces Lc3 accumulation at the contact site of omegasomes and the MAM (Figure 7). Although several factors such as PI3P, EPG-6, CapZ, and DFPC1 that influence omegasome formation have been identified (Axe et al., 2008; Lu et al., 2011; Mi et al., 2015; Mochizuki et al., 2013), LPAs such as 18:0-LPA are critical lipid metabolites that affect omegasome formation.

In conclusion, our findings indicate that saturated LPAs could perturb the autophagy machinery. As illustrated in our model (Figure 8K), we speculate that Gpat4 localizes on the MAM, utilizing excess SFAs by SCD inhibition and increases SFA intake and converts them into saturated LPAs, which are used as a lipid source for omegasome formation. However, excess production of saturated LPAs such as 18:0-LPA unbalances SFA-LPAs and UFA-LPAs on omegasomes, causing abnormal enlargement. Abnormally enlarged omegasomes containing excess saturated LPAs produce and accumulate isolation membranes, block autophagic flux, and cause vascular apoptosis and calcification. We previously reported that fully saturated PAs (i.e. 18:0/18:0-PA) generated through the Gpat4-Agpat3/5 reaction are responsible for SFA-mediated ER stress (Masuda et al., 2015). These results suggest that each SFA metabolite mediates a distinct pathway of SFA lipotoxicity. Taken together, Gpat4 could be a major therapeutic target for the treatment of lipotoxicity-induced chronic diseases such as vascular calcification.

Limitations of the Study

Although artifacts might arise due to the EM sample preparation, abnormal enlarged omegasome structures were only observed in cells treated with SFAs or SFA-LPAs but not vehicles. To ensure the results, the experiments have been at least triplicated. In addition, this study has revealed that GPAT4-generated SFA-LPAs indirectly affect autophagy through the generation of abnormal omegasomes. Follow-up studies will be required to determine whether GPAT4 and SFA-LPAs directly affect autophagosome formation.

Resource Availability

Lead Contact

Further information and requests for resources should be directed to and will be fulfilled by the Lead Contact, Makoto Miyazaki (makoto.miyazaki@cuanschutz.edu).

Materials Availability

All materials used and generated for this study are included in the published article and its supplementary information files or are available from the lead contact upon request.

METHODS

All methods can be found in the accompanying [Transparent Methods supplemental file](#).

DATA AND CODE AVAILABILITY

All data produced for this study are included in the published article and its supplementary information files or are available from the lead contact upon reasonable request.

SUPPLEMENTAL INFORMATION

Supplemental Information can be found online at <https://doi.org/10.1016/j.isci.2020.101105>.

ACKNOWLEDGMENTS

We thank B, Jennifer (for electron microscope study), R, Colman (for GPAT4 KO mice), and N, Mizushima (for GFP-LC3-RFP-LC3ΔG plasmid and conditional ATG5 KO mice). The authors' work was supported by grants from NIH United States, R01DK096030, R01HL117062, R01HL133545, and R01 HL132318 to M.M.

AUTHOR CONTRIBUTIONS

Conceptualization, Y.S. and M. Miyazaki; Methodology, Y.S., S.M.-A., and M. Miyazaki; Formal Analysis, Y.S., S.M.-A., and M. Miyazaki; Data Curation, Y.S., S.M.-A., and M. Miyazaki; Investigation, Y.S., S.M.-A., K.O., A.L.K., M. Masuda, and M. Miyazaki; Writing—Original Draft, Y.S. and M. Miyazaki; Writing—Review & Editing, Y.S., A.L.K., and M. Miyazaki; Visualization, Y.S., S.M.-A., and M. Miyazaki; Funding Acquisition, M. Miyazaki; Supervision, M. Miyazaki.

DECLARATION OF INTERESTS

All the authors declared no competing interests.

Received: August 19, 2019

Revised: December 16, 2019

Accepted: April 22, 2020

Published: May 22, 2020

REFERENCES

- Alwan, H.A., van Zoelen, E.J., and van Leeuwen, J.E. (2003). Ligand-induced lysosomal epidermal growth factor receptor (EGFR) degradation is preceded by proteasome-dependent EGFR deubiquitination. *J. Biol. Chem.* **278**, 35781–35790.
- An, H., Ordureau, A., Paulo, J.A., Shoemaker, C.J., Denic, V., and Harper, J.W. (2019). TEX264 is an endoplasmic reticulum-resident ATG8-interacting protein critical for ER remodeling during nutrient stress. *Mol. Cell* **74**, 891–908.e10.
- Anderson, E.K., Hill, A.A., and Hasty, A.H. (2012). Stearic acid accumulation in macrophages induces toll-like receptor 4/2-independent inflammation leading to endoplasmic reticulum stress-mediated apoptosis. *Arterioscler. Thromb. Vasc. Biol.* **32**, 1687–1695.
- Axe, E.L., Walker, S.A., Manifava, M., Chandra, P., Roderick, H.L., Habermann, A., Griffiths, G., and Ktistakis, N.T. (2008). Autophagosome formation from membrane compartments enriched in phosphatidylinositol 3-phosphate and dynamically connected to the endoplasmic reticulum. *J. Cell Biol.* **182**, 685–701.
- Blacher, J., Guerin, A.P., Pannier, B., Marchais, S.J., and London, G.M. (2001). Arterial calcifications, arterial stiffness, and cardiovascular risk in end-stage renal disease. *Hypertension* **38**, 938–942.
- Block, G.A., Raggi, P., Bellasi, A., Kooienga, L., and Spiegel, D.M. (2007). Mortality effect of coronary calcification and phosphate binder choice in incident hemodialysis patients. *Kidney Int.* **71**, 438–441.
- Brodeur, M.R., Bouvet, C., Barrette, M., and Moreau, P. (2013). Palmitic acid increases medial calcification by inducing oxidative stress. *J. Vasc. Res.* **50**, 430–441.
- Chino, H., Hatta, T., Natsume, T., and Mizushima, N. (2019). Intrinsically disordered protein TEX264 mediates ER-phagy. *Mol. Cell* **74**, 909–921.e906.
- Choi, S.E., Lee, S.M., Lee, Y.J., Li, L.J., Lee, S.J., Lee, J.H., Kim, Y., Jun, H.S., Lee, K.W., and Kang, Y. (2009). Protective role of autophagy in palmitate-induced INS-1 beta-cell death. *Endocrinology* **150**, 126–134.
- Dai, X.Y., Zhao, M.M., Cai, Y., Guan, Q.C., Zhao, Y., Guan, Y., Kong, W., Zhu, W.G., Xu, M.J., and Wang, X. (2013). Phosphate-induced autophagy counteracts vascular calcification by reducing matrix vesicle release. *Kidney Int.* **83**, 1042–1051.
- Dikic, I., and Elazar, Z. (2018). Mechanism and medical implications of mammalian autophagy. *Nat. Rev. Mol. Cell Biol.* **19**, 349–364.
- Durham, A.L., Speer, M.Y., Scatena, M., Giachelli, C.M., and Shanahan, C.M. (2018). Role of smooth muscle cells in vascular calcification: implications in atherosclerosis and arterial stiffness. *Cardiovasc. Res.* **114**, 590–600.
- Fagone, P., and Jackowski, S. (2009). Membrane phospholipid synthesis and endoplasmic reticulum function. *J. Lipid Res.* **50**(Suppl), S311–S316.
- Fujita, N., Itoh, T., Omori, H., Fukuda, M., Noda, T., and Yoshimori, T. (2008). The Atg16L complex specifies the site of LC3 lipidation for membrane biogenesis in autophagy. *Mol. Biol. Cell* **19**, 2092–2100.
- Gatica, D., Lahiri, V., and Klionsky, D.J. (2018). Cargo recognition and degradation by selective autophagy. *Nat. Cell Biol.* **20**, 233–242.
- Hailey, D.W., Rambold, A.S., Satpute-Krishnan, P., Mitra, K., Sougrat, R., Kim, P.K., and Lippincott-Schwartz, J. (2010). Mitochondria supply membranes for autophagosome biogenesis during starvation. *Cell* **141**, 656–667.
- Hamasaki, M., Furuta, N., Matsuda, A., Nezu, A., Yamamoto, A., Fujita, N., Oomori, H., Noda, T., Haraguchi, T., Hiraoka, Y., et al. (2013). Autophagosomes form at ER-mitochondria contact sites. *Nature* **495**, 389–393.
- Holthuis, J.C., and Menon, A.K. (2014). Lipid landscapes and pipelines in membrane homeostasis. *Nature* **510**, 48–57.
- Hsiao, Y.H., Lin, C.I., Liao, H., Chen, Y.H., and Lin, S.H. (2014). Palmitic acid-induced neuron cell cycle G2/M arrest and endoplasmic reticular stress through protein palmitoylation in SH-SY5Y human neuroblastoma cells. *Int. J. Mol. Sci.* **15**, 20876–20899.
- Ichimura, Y., Kirisako, T., Takao, T., Satomi, Y., Shimonishi, Y., Ishihara, N., Mizushima, N., Tanida, I., Kominami, E., Ohsumi, M., et al. (2000). A ubiquitin-like system mediates protein lipidation. *Nature* **408**, 488–492.
- Itakura, E., Kishi-Itakura, C., and Mizushima, N. (2012). The hairpin-type tail-anchored SNARE syntaxin 17 targets to autophagosomes for fusion with endosomes/lysosomes. *Cell* **151**, 1256–1269.
- Itakura, E., Kishi, C., Inoue, K., and Mizushima, N. (2008). Beclin 1 forms two distinct phosphatidylinositol 3-kinase complexes with mammalian Atg14 and UVRAG. *Mol. Biol. Cell* **19**, 5360–5372.
- Itakura, E., and Mizushima, N. (2010). Characterization of autophagosome formation site by a hierarchical analysis of mammalian Atg proteins. *Autophagy* **6**, 764–776.
- Kabeya, Y., Mizushima, N., Yamamoto, A., Oshitani-Okamoto, S., Ohsumi, Y., and Yoshimori, T. (2004). LC3, GABARAP and GATE16 localize to autophagosomal membrane depending on form-II formation. *J. Cell Sci.* **117**, 2805–2812.
- Kaizuka, T., Morishita, H., Hama, Y., Tsukamoto, S., Matsui, T., Toyota, Y., Kodama, A., Ishihara, T., Mizushima, T., and Mizushima, N. (2016). An autophagic flux probe that releases an internal control. *Mol. Cell* **64**, 835–849.
- Khaminets, A., Heinrich, T., Mari, M., Grumati, P., Huebner, A.K., Akutsu, M., Liebmann, L., Stolz, A., Nietzsche, S., Koch, N., et al. (2015). Regulation of endoplasmic reticulum turnover by selective autophagy. *Nature* **522**, 354–358.
- Khan, M.J., RizwanAlam, M., Waldeck-Weiermair, M., Karsten, F., Groschner, L., Riederer, M., Hallstrom, S., Rockenfeller, P., Konya, V., Heinemann, A., et al. (2012). Inhibition of autophagy rescues palmitic acid-induced necroptosis of endothelial cells. *J. Biol. Chem.* **287**, 21110–21120.
- Kohno, S., Shiozaki, Y., Keenan, A.L., Miyazaki-Anzai, S., and Miyazaki, M. (2019). An N-terminal-truncated isoform of FAM134B (FAM134B-2) regulates starvation-induced hepatic selective ER-phagy. *Life Sci. Alliance* **2**, e201900340.

- Kovacic, J.C., Moreno, P., Hachinski, V., Nabel, E.G., and Fuster, V. (2011a). Cellular senescence, vascular disease, and aging: Part 1 of a 2-part review. *Circulation* 123, 1650–1660.
- Kovacic, J.C., Moreno, P., Nabel, E.G., Hachinski, V., and Fuster, V. (2011b). Cellular senescence, vascular disease, and aging: part 2 of a 2-part review: clinical vascular disease in the elderly. *Circulation* 123, 1900–1910.
- Lamark, T., Svenning, S., and Johansen, T. (2017). Regulation of selective autophagy: the p62/SQSTM1 paradigm. *Essays Biochem.* 61, 609–624.
- Lamb, C.A., Yoshimori, T., and Tooze, S.A. (2013). The autophagosome: origins unknown, biogenesis complex. *Nat. Rev. Mol. Cell Biol.* 14, 759–774.
- Las, G., Serada, S.B., Wikstrom, J.D., Twig, G., and Shirihai, O.S. (2011). Fatty acids suppress autophagic turnover in beta-cells. *J. Biol. Chem.* 286, 42534–42544.
- Leidal, A.M., Levine, B., and Debnath, J. (2018). Autophagy and the cell biology of age-related disease. *Nat. Cell Biol.* 20, 1338–1348.
- Levine, B., and Kroemer, G. (2008). Autophagy in the pathogenesis of disease. *Cell* 132, 27–42.
- Listenberger, L.L., Han, X., Lewis, S.E., Cases, S., Farese, R.V., Jr., Ory, D.S., and Schaffer, J.E. (2003). Triglyceride accumulation protects against fatty acid-induced lipotoxicity. *Proc. Natl. Acad. Sci. U S A* 100, 3077–3082.
- Liu, J., Chang, F., Li, F., Fu, H., Wang, J., Zhang, S., Zhao, J., and Yin, D. (2015). Palmitate promotes autophagy and apoptosis via activation of the DNA damage response and senescence-associated secretory phenotype in vascular smooth muscle cells. *Circ. Res.* 112, e99–e109.
- Lu, Q., Yang, P., Huang, X., Hu, W., Guo, B., Wu, F., Lin, L., Kovacs, A.L., Yu, L., and Zhang, H. (2011). The WD40 repeat PtdIns(3)P-binding protein EPG-6 regulates progression of omegasomes to autophagosomes. *Dev. Cell* 21, 343–357.
- Maiuri, M.C., and Kroemer, G. (2019). Therapeutic modulation of autophagy: which disease comes first? *Cell Death Differ.* 26, 680–689.
- Man, W.C., Miyazaki, M., Chu, K., and Ntambi, J. (2006). Colocalization of SCD1 and DGAT2: implying preference for endogenous monounsaturated fatty acids in triglyceride synthesis. *J. Lipid Res.* 47, 1928–1939.
- Mari, M., Griffith, J., Rieter, E., Krishnappa, L., Klionsky, D.J., and Reggiori, F. (2010). An Atg9-containing compartment that functions in the early steps of autophagosome biogenesis. *J. Cell Biol.* 190, 1005–1022.
- Masuda, M., Miyazaki-Anzai, S., Keenan, A.L., Okamura, K., Kendrick, J., Chonchol, M., Offermanns, S., Ntambi, J.M., Kuro, O.M., and Miyazaki, M. (2015). Saturated phosphatidic acids mediate saturated fatty acid-induced vascular calcification and lipotoxicity. *J. Clin. Invest.* 125, 4544–4558.
- Masuda, M., Ting, T.C., Levi, M., Saunders, S.J., Miyazaki-Anzai, S., and Miyazaki, M. (2012). Activating transcription factor 4 regulates stearate-induced vascular calcification. *J. Lipid Res.* 53, 1543–1552.
- Matsunaga, K., Saitoh, T., Tabata, K., Omori, H., Satoh, T., Kurotori, N., Maejima, I., Shirahama-Noda, K., Ichimura, T., Isobe, T., et al. (2009). Two Beclin 1-binding proteins, Atg14L and Rubicon, reciprocally regulate autophagy at different stages. *Nat. Cell Biol.* 11, 385–396.
- Matsushita, M., Suzuki, N.N., Obara, K., Fujioka, Y., Ohsumi, Y., and Inagaki, F. (2007). Structure of Atg5-Atg16, a complex essential for autophagy. *J. Biol. Chem.* 282, 6763–6772.
- Mei, S., Ni, H.M., Manley, S., Bockus, A., Kassel, K.M., Luyendyk, J.P., Copple, B.L., and Ding, W.X. (2011). Differential roles of unsaturated and saturated fatty acids on autophagy and apoptosis in hepatocytes. *J. Pharmacol. Exp. Ther.* 339, 487–498.
- Mi, N., Chen, Y., Wang, S., Chen, M., Zhao, M., Yang, G., Ma, M., Su, Q., Luo, S., Shi, J., et al. (2015). CapZ regulates autophagosomal membrane shaping by promoting actin assembly inside the isolation membrane. *Nat. Cell Biol.* 17, 1112–1123.
- Mitroi, D.N., Karunakaran, I., Graler, M., Saba, J.D., Ehninger, D., Ledesma, M.D., and van Echten-Deckert, G. (2017). SGPL1 (sphingosine phosphatase 1) modulates neuronal autophagy via phosphatidylethanolamine production. *Autophagy* 13, 885–899.
- Miyazaki, M., and Ntambi, J.M. (2003). Role of stearoyl-coenzyme A desaturase in lipid metabolism. *Prostaglandins Leukot. Essent. Fatty Acids* 68, 113–121.
- Mizushima, N., and Komatsu, M. (2011). Autophagy: renovation of cells and tissues. *Cell* 147, 728–741.
- Mizushima, N., Kuma, A., Kobayashi, Y., Yamamoto, A., Matsubae, M., Takao, T., Natsume, T., Ohsumi, Y., and Yoshimori, T. (2003). Mouse Apg16L, a novel WD-repeat protein, targets to the autophagic isolation membrane with the Apg12-Apg5 conjugate. *J. Cell Sci.* 116, 1679–1688.
- Mochizuki, Y., Ohashi, R., Kawamura, T., Iwanari, H., Kodama, T., Naito, M., and Hamakubo, T. (2013). Phosphatidylinositol 3-phosphatase myotubularin-related protein 6 (MTMR6) is regulated by small GTPase Rab1B in the early secretory and autophagic pathways. *J. Biol. Chem.* 288, 1009–1021.
- Nussenzweig, S.C., Verma, S., and Finkel, T. (2015). The role of autophagy in vascular biology. *Circ. Res.* 116, 480–488.
- Ogasawara, Y., Itakura, E., Kono, N., Mizushima, N., Arai, H., Nara, A., Mizukami, T., and Yamamoto, A. (2014). Stearoyl-CoA desaturase 1 activity is required for autophagosome formation. *J. Biol. Chem.* 289, 23938–23950.
- Ohashi, Y., and Munro, S. (2010). Membrane delivery to the yeast autophagosome from the Golgi-endosomal system. *Mol. Biol. Cell* 21, 3998–4008.
- Park, J.S., Lee, D.H., Lee, Y.S., Oh, E., Bae, K.H., Oh, K.J., Kim, H., and Bae, S.H. (2019). Dual roles of ULK1 (unc-51 like autophagy activating kinase 1) in cytoprotection against lipotoxicity. *Autophagy* 16, 1–20.
- Petiot, A., Ogier-Denis, E., Blommaert, E.F., Meijer, A.J., and Codogno, P. (2000). Distinct classes of phosphatidylinositol 3'-kinases are involved in signaling pathways that control macroautophagy in HT-29 cells. *J. Biol. Chem.* 275, 992–998.
- Piccolis, M., Bond, L.M., Kampmann, M., Pulimeno, P., Chitruju, C., Jayson, C.B.K., Vaites, L.P., Boland, S., Lai, Z.W., Gabriel, K.R., et al. (2019). Probing the global cellular responses to lipotoxicity caused by saturated fatty acids. *Mol. Cell* 74, 32–44.e8.
- Polson, H.E., de Lartigue, J., Rigden, D.J., Reedijk, M., Urbe, S., Clague, M.J., and Tooze, S.A. (2010). Mammalian Atg18 (WIP1) localizes to omegasome-anchored phagophores and positively regulates LC3 lipidation. *Autophagy* 6, 506–522.
- Proudfoot, D., Skepper, J.N., Hegyi, L., Bennett, M.R., Shanahan, C.M., and Weissberg, P.L. (2000). Apoptosis regulates human vascular calcification in vitro: evidence for initiation of vascular calcification by apoptotic bodies. *Circ. Res.* 87, 1055–1062.
- Puri, C., Renna, M., Bento, C.F., Moreau, K., and Rubinsztein, D.C. (2013). Diverse autophagosome membrane sources coalesce in recycling endosomes. *Cell* 154, 1285–1299.
- Ravikumar, B., Moreau, K., Jahreiss, L., Puri, C., and Rubinsztein, D.C. (2010). Plasma membrane contributes to the formation of pre-autophagosomal structures. *Nat. Cell Biol.* 12, 747–757.
- Ren, J., and Zhang, Y. (2018). Targeting autophagy in aging and aging-related cardiovascular diseases. *Trends Pharmacol. Sci.* 39, 1064–1076.
- Rockenfeller, P., Koska, M., Pietrocola, F., Minois, N., Knittelfelder, O., Sica, V., Franz, J., Carmona-Gutierrez, D., Kroemer, G., and Madeo, F. (2015). Phosphatidylethanolamine positively regulates autophagy and longevity. *Cell Death Differ.* 22, 499–508.
- Rogers, M.A., and Aikawa, E. (2019). Cardiovascular calcification: artificial intelligence and big data accelerate mechanistic discovery. *Nat. Rev. Cardiol.* 16, 261–274.
- Shanahan, C.M., Crouthamel, M.H., Kapustin, A., and Giachelli, C.M. (2011). Arterial calcification in chronic kidney disease: key roles for calcium and phosphate. *Circ. Res.* 109, 697–711.
- Sun, Q., Fan, W., Chen, K., Ding, X., Chen, S., and Zhong, Q. (2008). Identification of Barkor as a mammalian autophagy-specific factor for Beclin 1 and class III phosphatidylinositol 3-kinase. *Proc. Natl. Acad. Sci. U S A* 105, 19211–19216.

Tan, S.H., Shui, G., Zhou, J., Li, J.J., Bay, B.H., Wenk, M.R., and Shen, H.M. (2012). Induction of autophagy by palmitic acid via protein kinase C-mediated signaling pathway independent of mTOR (mammalian target of rapamycin). *J. Biol. Chem.* **287**, 14364–14376.

Tan, S.H., Shui, G., Zhou, J., Shi, Y., Huang, J., Xia, D., Wenk, M.R., and Shen, H.M. (2014). Critical role of SCD1 in autophagy regulation via lipogenesis and lipid rafts-coupled AKT-FOXO1 signaling pathway. *Autophagy* **10**, 226–242.

Tanida, I., Sou, Y.S., Ezaki, J., Minematsu-Ikeguchi, N., Ueno, T., and Kominami, E. (2004). HsAtg4B/HsApg4B/autophagin-1 cleaves the carboxyl termini of three human Atg8 homologues and delipidates microtubule-associated protein light chain 3- and GABAA receptor-associated protein-phospholipid conjugates. *J. Biol. Chem.* **279**, 36268–36276.

Tsuyoyama, K., Koyama-Honda, I., Sakamaki, Y., Koike, M., Morishita, H., and Mizushima, N. (2016). The ATG conjugation systems are important for degradation of the inner autophagosomal membrane. *Science* **354**, 1036–1041.

Uematsu, M., Nishimura, T., Sakamaki, Y., Yamamoto, H., and Mizushima, N. (2017). Accumulation of undegraded autophagosomes by expression of dominant-negative STX17 (syntaxin 17) mutants. *Autophagy* **13**, 1452–1464.

Ueno, T., and Komatsu, M. (2017). Autophagy in the liver: functions in health and disease. *Nat. Rev. Gastroenterol. Hepatol.* **14**, 170–184.

Vance, J.E. (1990). Phospholipid synthesis in a membrane fraction associated with mitochondria. *J. Biol. Chem.* **265**, 7248–7256.

Wen, H., Gris, D., Lei, Y., Jha, S., Zhang, L., Huang, M.T., Brickey, W.J., and Ting, J.P. (2011). Fatty acid-induced NLRP3-ASC inflammasome activation interferes with insulin signaling. *Nat. Immunol.* **12**, 408–415.

Yamamoto, H., Kakuta, S., Watanabe, T.M., Kitamura, A., Sekito, T., Kondo-Kakuta, C., Ichikawa, R., Kinjo, M., and Ohsumi, Y. (2012). Atg9 vesicles are an important membrane source during early steps of autophagosome formation. *J. Cell Biol.* **198**, 219–233.

Yoshii, S.R., and Mizushima, N. (2017). Monitoring and measuring autophagy. *Int. J. Mol. Sci.* **18**, 1865.

Zhao, Y., Zhao, M.M., Cai, Y., Zheng, M.F., Sun, W.L., Zhang, S.Y., Kong, W., Gu, J., Wang, X., and Xu, M.J. (2015). Mammalian target of rapamycin signaling inhibition ameliorates vascular calcification via Klothoupregulation. *Kidney Int.* **88**, 711–721.

Zhong, Y., Wang, Q.J., Li, X., Yan, Y., Backer, J.M., Chait, B.T., Heintz, N., and Yue, Z. (2009). Distinct regulation of autophagic activity by Atg14L and Rubicon associated with Beclin 1-phosphatidylinositol-3-kinase complex. *Nat. Cell Biol.* **11**, 468–476.

Zhu, X.G., Nicholson Puthenveedu, S., Shen, Y., La, K., Ozlu, C., Wang, T., Klompstra, D., Gultekin, Y., Chi, J., Fidelin, J., et al. (2019). CHP1 regulates compartmentalized glycerolipid synthesis by activating GPAT4. *Mol. Cell* **74**, 45–58 e47.

Zou, J., Zhang, C., Marjanovic, J., Kisseleva, M.V., Majerus, P.W., and Wilson, M.P. (2012). Myotubularin-related protein (MTMR) 9 determines the enzymatic activity, substrate specificity, and role in autophagy of MTMR8. *Proc. Natl. Acad. Sci. U S A* **109**, 9539–9544.

iScience, Volume 23

Supplemental Information

GPAT4-Generated Saturated LPAs Induce Lipotoxicity through Inhibition of Autophagy by Abnormal Formation of Omegasomes

Yuji Shiozaki, Shinobu Miyazaki–Anzai, Kayo Okamura, Audrey L. Keenan, Masashi Masuda, and Makoto Miyazaki

TRANSPARENT METHODS

Animals

SMC-*Scd1/2* KO mice, *Atg5* conditional KO mice, *SMMHC-CreER^(T2)* mice, *Gpat4* KO mice and CKD mice were used (Hara et al., 2006; Masuda et al., 2015; Masuda et al., 2016; Masuda et al., 2012; Miyazaki-Anzai et al., 2010; Miyazaki et al., 2007; Nagle et al., 2008; Vergnes et al., 2006). To generate VSMC-specific *Atg5* KO mice, *Atg5* conditional KO mice were intercrossed with *SMMHC-CreER^(T2)* mice to obtain *SMMHC-CreER^(T2); Atg5^(lox/lox)* mice. *Atg5* conditional KO mice were used as control mice. VSMC-*Scd1/2* KO; *Gpat4* KO mice were generated by crossing SMC-*Scd1/2* KO and *Gpat4* KO mice. Since the *SMMHC-CreER^(T2)* transgene was inserted on the Y chromosome, only males were used in this study. Five-week-old males were subjected to 5/6 nephrectomy to induce CKD-dependent vascular calcification as previously described (Masuda et al., 2015; Masuda et al., 2016; Miyazaki-Anzai et al., 2010). One week after the surgery, CKD mice were injected intraperitoneally with tamoxifen (1 mg/kg body weight) in vegetable oil. After the injections, the mice were maintained on a special diet (TD10364) for 6 weeks. All of the mouse strains were backcrossed at least 10 times with DBA/2J.

Histological analysis

Calcified lesions in the aortic sinus were analyzed as previously described using either Alizarin red or von Kossa staining. Apoptotic cells in the aortas were detected using an In Situ Cell Death Detection Kit (Roche). At least 5 sections from each sample were analyzed (Masuda et al., 2015; Masuda et al., 2016; Masuda et al., 2013; Miyazaki-Anzai et al., 2010; Miyazaki-Anzai et al., 2014; Shiozaki et al., 2018).

Cell cultures

Human VSMCs and mouse VSMCs were purchased from Applied Biological Materials (T0515, Richmond, Canada). Mouse VSMCs (MOVAS-1), HeLa cells and NIH3T3 cells were purchased from American Type Culture Collection (ATCC). VSMCs were maintained in DMEM containing 10% fetal bovine serum with 100 U/ml penicillin and 100 µg/ml streptomycin. VSMCs were treated with complete media (with FBS and amino acids) or EBSS (for starvation) and 250 µM fatty acids such as C18:0 or 200 nM bafilomycin A1 for 2 or 6 hours to prepare for total cell lysates.

RNA analysis

Total RNA was isolated using Direct-zol RNA kit (Zymo Research). cDNA was synthesized from 500 ng total RNA using High-Capacity cDNA Reverse Transcription Kit (Applied Biological Materials Inc). qRT-PCR was performed using an Applied Biosystems StepOne Plus qPCR

instrument with SYBR™ Select Master Mix according to manufacturer's instructions (Masuda et al., 2015; Shiozaki et al., 2018).

Preparation of lentiviral particles and CRISPR-Cas9 system-based gene knockout of the *Atg5* gene

Scrambled (Applied Biological Materials Inc, Richmond, Canada) or *Atg5* gene sgRNA in pLenti-U6-sgRNA-SFFV-Cas9-2A-Puro plasmid (Applied Biological Materials Inc), including the Cas9 coding sequence in the lentiviral sequence region, were purchased. HEK293T cells were seeded at 6×10^5 cells/well in 6-well plates, grown overnight, and then transfected with 300 ng psPAX2, 100 ng pMD2 and 400 ng of each sgRNA CRISPR Cas9 lentivirus plasmid (plasmid amount rate 3:1:4) using Turbofect transfection reagent (Thermo Fisher Scientific). Media was changed to new media, and media containing lentiviral particles was collected 2 days later. Lentiviral media was centrifuged once at $1500 \times g$ for 3 minutes and the supernatant was collected. MOVAS cells were seeded in 6-well plates and infected 24 hours later with each lentiviral media in the presence of $10 \mu\text{g/ml}$ polybrene. Cells were treated with $3 \mu\text{g/ml}$ puromycin for selection of infected cells. Total RNA of heterogeneous cells was collected and cDNA synthesis was conducted from the RNA template, followed by high resolution melting analysis (Bassett et al., 2013) with a StepOne Plus qPCR instrument (Applied Biosystems) to check for mutations occurring on regions around *Atg5* sgRNA target sequence. Heterogeneous cells with gene mutations were plated at 0.5 cells/well in a 96-well plate to obtain a single cell clone. Next, total RNA of each single cell-derived clone was collected to check for mutations using high resolution melting qRT-PCR, and each mutated sequence was analyzed by DNA sequencing (Eurofins Genomics Company). Protein from gene edited clones was prepared and analyzed by immunoblot analysis to determine whether gene knockout was complete.

Generation of fluorescence protein conjugated LC3, p62, Stx17, DFPC1 and FLAG-GPAT4 overexpressed and acyltransferase knockdown VSMCs

Retroviral plasmid vectors of pMRX-IP-GFP-LC3-RFP-LC3 Δ G (#84572), pMXs-puro GFP-p62 (#38277), pMRX-IP GFP-Stx17 WT (#45909) and pMXs-puro GFP-DFPC1 (#38269) were purchased from Addgene (Cambridge, MA). N-terminal FLAG-tag and C-terminal tdTomato fluorescent protein-fused human GPAT4 was cloned into pLenti CMV. HEK293T cells were plated and grown overnight. Cells were transfected with the retroviral vectors pUMV3 and VSVG as described above using Turbofect transfection reagent (Thermo Fisher Scientific). Media was changed to new media, and media containing retroviral particles was collected 2 days later. MOVAS cells were seeded in 6-well plates and infected 24 hours later with each lentiviral media in the presence of $10 \mu\text{g/ml}$ polybrene. Cells were treated with $3 \mu\text{g/ml}$ puromycin for selection

of infected cells. Fluorescence of MOVAS colonies was observed by an EVOS M5000 microscope (Thermo Fisher Scientific) and bright colonies were transferred to new a dish for the experiments. Acyltransferase knockdown VSMCs were described in our previous paper (Masuda et al., 2015).

Fluorescence microscopy analysis

Fluorescence protein overexpressed or wild-type VSMCs were plated on Lab-Tek® chamber slides (Thermo #154534) with poly-L-lysine coating. After 24 hours, VSMCs were treated with complete media or EBSS (starvation media) and 200 μ M fatty acids such as C18:0, 3 μ M CAY10566 and 50 μ M C18:0, 100 μ M 18:0-LPA, 100 μ M 18:0/18:0-PA or 200 nM bafilomycin A1 for 2 or 6 hours. Before treatment with leupeptin and pepstatin A, VSMCs were pre-incubated with 10 μ g/ml leupeptin and 10 μ g/ml pepstatin A for 6 hours. VSMCs were then washed with 1x PBS, followed by fixation with 4% paraformaldehyde/1x PBS for 10 minutes. Fixed VSMCs were washed with 1x PBS and quenched with 20 mM glycine/PBS for 10 minutes. VSMCs were permeabilized with 50 μ g/ml digitonin/0.1%gelatin/PBS for 10 minutes or 0.05% saponin/PBS for 30 minutes (for staining of KDEL). VSMCs were then blocked with 0.1%gelatin/PBS or 1%BSA/PBS for 30 minutes and treated with the following primary antibodies for 1 hour at room temperature.: Lc3 rabbit polyclonal (PM036, MBL), Lc3 mouse monoclonal (M152-3, MBL), LAMP1 (1D4B, DSHB at University of Iowa), WIPI2 (SAB4200400, Sigma-Aldrich), FLAG M2 (F1804, Sigma-Aldrich), KDEL (10C3, MBL), RCAS1 (D2B6N, Cell Signaling Technology), Tomm20 (FL-145, Santacruz) and Calnexin (A303-696A, Bethyl laboratory). VSMCs were washed with 0.1% gelatin/PBS or 0.01% saponin/PBS and reacted with Alexa Fluor dye conjugated secondary antibody for 1 hour at room temperature. VSMCs were washed with 0.1% gelatin/PBS or 0.01% saponin/PBS and mounted with VECTASHIELD® Antifade Mounting Medium with DAPI (VECTOR laboratories) on glass slides. For lipid droplet staining, VSMCs were fixed with 4 % PFA/PBS for 10 minutes, washed with 1x PBS and incubated with HCS LipidTox™ Red neutral lipid stain (Thermo Fisher Scientific) for 1 hour. For Mtmr gene knockdown experiments, stable VSMCs expressing GFP-DFCP1 were transfected with 20 nM negative control or Mtmr siRNAs. After 24 hours of transfection, VSMCs were treated with EBSS for 2 hours and fixed with 4% paraformaldehyde. Prepared samples were observed with an Olympus FluoView™ FV1000 confocal microscope (Olympus). Images were gained at 1024x1024 pixel resolution and used for measuring fluorescent puncta or areas. Quantification of data was performed using ImageJ software.

GFP-LC3-RFP-LC3 Δ G microplate assay

Wild-type (as background) or stable VSMCs expressing GFP-LC3-RFP-LC3 Δ G were plated at

55000 cells/well in poly-L-lysine coated 96-well microplate and grown overnight. For Gpat4 siRNA knockdown, VSMCs were plated at 30000 cells/well in 96 well microplates, grown overnight and then transfected with 50 nM negative control or Gpat4 siRNA. VSMCs were co-treated with EBSS (starvation media) and 300 μ M fatty acids, 100 μ M 18:0-LPA or 100 nM bafilomycin A1 for 6 hours. After treatment, VSMCs were fixed with 4% paraformaldehyde/PBS for 15 minutes. VSMCs were washed twice with 1x PBS and 100 μ l PBS/well was added for measurement. GFP and RFP fluorescence were measured using a BioTek Synergy2 Multi-Detection Microplate Reader (BioTek, Winooski, VT, USA).

Electron microscopy

VSMCs were plated in Permax dishes (#70350, Electron Microscopy Science) and grown overnight. VSMCs were co-treated with EBSS and BSA (Vehicle) or 300 μ M C18:0 for 2 hours. Media was removed, and fixative solution (2% paraformaldehyde/2.5% glutaraldehyde in 0.1M cacodylate buffer) was added to VSMCs. After fixation for 1 hour at room temperature, fixative solution was removed. VSMCs were washed with 0.1 M cacodylate buffer. VSMCs were secondary fixed, stained and coated by the University of Colorado-Denver Anschutz Medical Campus Electron Microscopy Center. Sections were imaged on a FEI Tecnai G2 transmission electron microscope (Hillsboro, OR, USA) with an AMT digital camera (Woburn, MA, USA).

Measurement of PI3P

Lipid extraction and measurement of PI3P with PI3P Mass ELISA kit (Echelon Bioscience Inc.) were performed according to manufacturer's instructions and previous reports (Li et al., 2017; Rohatgi et al., 2015; Zhong et al., 2014). VSMCs were plated at 35×10^5 cells/dish in 10 cm plates for PI3P extraction and BCA assay.

Immunoblot analysis

Cell and tissue lysates were prepared using RIPA buffer (150 mM NaCl, 1% Nonidet P-40, 0.5% sodium deoxycholate, 0.1% SDS, 50 mM Tris, pH 8.0). Cells were disrupted by pipetting 10-15 times, centrifuged at 13800 x g for 10 minutes at 4°C and the supernatant was collected for total cell lysates. The samples were separated by SDS-PAGE, transferred to a nitrocellulose membrane, and immunoblotted with the following antibodies: p62 (#5114), ATF4 (D4B8), CHOP (L63F7), BiP (C50B12), Atg5 (D5F5U), EGFR (D38B1), Beclin-1 (D40C5), Vps34 (D9A5) and RCAS1 (D2B6N) from Cell Signaling Technology, Gapdh (V-18), GFP (B-2) and Tomm20 (FL-145) from Santa Cruz Biotechnology, LAMP1 (1D4B) from Developmental Studies Hybridoma Bank (University of Iowa), Stx17 (A305-750A) and Calnexin (A303-696A) from Bethyl Laboratories, Lc3b (NB100-2220), TEX264 (NBP1-89866) and Fac14 (NBP2-16401) from Novus Biologicals,

β -Actin (66009) from Proteintech and Fam134b was developed as described in our previous report (Kohno et al., 2019). Samples were visualized using horseradish peroxidase coupled to appropriate secondary antibodies with enhancement by an ECL detection kit (Thermo Fisher Scientific).

Calcium content in cultured cells and aortas

For evaluation of SFA-induced vascular calcification, VSMCs were plated at 1.0×10^5 cells/well in 12-well plate and grown overnight. VSMCs were treated with BSA (vehicle), 200 μ M C18:0, 20 μ M 18:0-LPA, 200 μ M C18:0 and 200 μ M C18:1 or 200 μ M C18:0 and 20 μ M 18:1-LPA with 2.6 mM Pi every 2 days for 6 days. VSMCs were incubated with 0.6 N HCl overnight at 4 °C. After incubation, 0.6 N HCl was collected to measure calcium content, and then VSMCs were lysised with 0.1 N NaOH/0.1%SDS to measure protein concentration by BCA assay. Aortas were collected from mice and then stored at -20°C. Dried aorta was defatted with chloroform and methanol (2:1) for 48 hours and dehydrated with acetone for three hours. The dried samples were incinerated to ashes at 600°C for 24 hours using an electric muffle furnace (Thermo Scientific), then extracted with 0.6 N HCl. Calcium contents from cultured cells and aortas was quantified by using the o-cresolphthalein method. In addition, VSMCs were stained with Alizarin red to identify calcium deposits after 6 days of Pi treatment. (Masuda et al., 2015; Masuda et al., 2016; Masuda et al., 2012).

Isolation of mitochondria associated membrane (MAM) of VSMCs

MAM fractions were prepared according to previous reports (Man et al., 2006; Wieckowski et al., 2009). VSMCs were prepared in 24 x 150 mm dishes per experimental group. VSMCs at 80–90% confluency were starved in EBSS with BSA (vehicle) or 300 μ M C18:0 for 2 hours. After treatment with EBSS with or without SFAs, VSMCs were collected in conical tubes with ice-cold 1x PBS. Cells were centrifuged at 600 x g for 5 min at 4 °C. The supernatant was discarded and cells were washed with 1x PBS. Cells were centrifuged at 600 x g, the supernatant was discarded, and cells were resuspended in isolation buffer (225 mM mannitol, 75 mM sucrose, 0.1 mM EGTA and 30 mM Tris-HCl, pH 7.4) and homogenized using a Teflon pestle at 3000 rpm for 50 strokes at 4 °C. Homogenized cells were centrifuged at 600 x g for 10 min at 4 °C two times to remove pellets of unbroken cells and nuclei. The collected supernatant was centrifuged at 7000 x g for 10 min at 4 °C. The pellet (crude mitochondria) was resuspended in isolation buffer-2 (225 mM mannitol, 75 mM sucrose and 30 mM Tris-HCl, pH7.4) using a loose fitting glass/Teflon Potter Elvehjem homogenizer with 2 to 3 strokes by hand. The supernatant was centrifuged at 100000 x g for 1 hour at 4 °C (70 Ti rotor, Beckman Coulter) to collect microsomal (pellet) and cytosolic (supernatant) fractions. Crude mitochondria was centrifuged and resuspended in isolation buffer-

2 as described above to wash. Mitochondria was centrifuged at 10000 x g for 10 min at 4 °C, supernatant was discarded and the pellet was resuspended in 2 ml mitochondria resuspension buffer (MRB; 250 mM mannitol, 25 mM HEPES, pH 7.4 and 0.5 mM EGTA). The resuspended mitochondria fraction was gently placed on top of 8 ml Percoll media (225 mM mannitol, 25 mM HEPES pH 7.4, 1 mM EGTA and 30 % Percoll (v/v)) in a polypropylene ultracentrifuge tube (#331372, Beckman Coulter) and topped with MRB (3.5 ml approximate total volume) until 2-3 mm from the top of the tube, and was centrifuged at 95000 x g for 30 min at 4 °C with an SW41 Ti rotor (Beckman Coulter). After centrifuging, MAM fractions (the thin white band 1/2-2/3 from the bottom of the tube) and mitochondria fractions (the brown fraction at the bottom of the tube) were collected in separate tubes. Each fraction was diluted ten times with MRB and centrifuged at 6300 x g for 10 min at 4 °C. Mitochondria fractions (pellet) were centrifuged at 6300 x g for 10 min at 4 °C and the pellet was collected as pure mitochondrial fractions and resuspended in MRB. MAM fractions (supernatant) were transferred to polycarbonate tubes with caps and centrifuged at 100000 x g for 1 hour at 4 °C (70 Ti rotor, Beckman Coulter). The supernatant containing mitochondrial fractions was discarded and the pellet was collected as MAM fractions and resuspended in MRB.

Optiprep density gradient centrifuge and lysophosphatidic acid analysis

The Optiprep density gradient centrifuge fraction method was described in previous reports (Itakura and Mizushima, 2010; Kohno et al., 2019; Nishimura et al., 2017; Uematsu et al., 2017). Stable VSMCs expressing GFP-DFCP1 were cultured in 4 x 15 cm dishes overnight. At 80–90% confluency, VSMCs were treated with EBSS and BSA or 300 μM C18:0 for 2 hours. VSMCs were washed with 1x PBS twice and collected into conical tubes with 1x PBS. VSMCs were centrifuged at 600 x g for 5 minutes at 4 °C and washed twice with 1x PBS. After centrifuging at 600 x g for 5 minutes, VSMCs were resuspended in homogenate buffer (250 mM sucrose, 20 mM HEPES-KOH, pH 7.4 and 1 mM EDTA with protease inhibitor). VSMCs were homogenized using a 25G-gauge syringe with 20 strokes on ice. Homogenized VSMCs were centrifuged at 3000 x g for 10 minutes at 4 °C. The supernatant was transferred to a new tube twice to discard unbroken cells and nuclei. The protein concentration of the supernatant was measured with a BCA protein assay. Supernatant containing 1.5 mg protein was adjusted to 1.2 ml volume with homogenate buffer, mixed with 1.2 ml 50% Optiprep (1114542, Sigma-Aldrich) and transferred to the bottom of an ultracentrifuge tube (#331372, Beckman Coulter). Next, 1.8 ml in 20% Optiprep (diluted with homogenate buffer), 2 ml in 15% Optiprep, 2 ml in 10% Optiprep, 2 ml in 5% Optiprep and 2.2 ml in 0% Optiprep were sequentially layered in the ultracentrifuge tube. The gradients were centrifuged at 150,900 x g using an SW41 Ti rotor (Beckman Coulter) for 3 hours at 4 °C, and then 14 fractions (0.85 ml each) were collected from the top. For measurement of

lysophosphatidic amount, 400 µl from each fraction was separated to new tubes.

LS/MS lipidomic analysis

LPAs in the MAM fraction and membrane fractions from Optiprep were quantified (Masuda et al., 2015). In brief, lipid extraction was performed by LC ESI-MS/MS using a Shimadzu LC-20AD liquid chromatography (HPLC) system and an Applied Biosystems 3200 qTrap mass spectrometer with a turbo-ion spray source (350°C). HPLC was performed on a Zorbax C18, 1.8 µm, 50 x 2.1 mm column (Agilent Technology). Solvents A and B consisted of tetrahydrofuran:methanol:water (30:20:50 and 75:20:5, respectively), both containing 10 mM ammonium formate. Columns were heated to 50°C. Lipids were separated under gradient conditions (300 µl/min): 0% solvent B to 100% solvent B for 10.5 minutes, returned to 0% solvent B at 11 minutes and maintained for 5 minutes. LPA was analyzed with a negative ion mode. The detailed mass spectrometry conditions such as collision energy, declustering potential and mass transition are available upon request. The 17:0-LPA internal standard was purchased from Avanti Polar Lipid.

Statistics

Data were collected from more than 2 independent experiments and are reported as the mean ± SEM. Statistical analysis was performed using a 2-tailed Student's t test for 2 group comparisons and a 1-way ANOVA with a Student-Newman post-hoc test or 2-way ANOVA for multigroup comparison. Significance was accepted at $P < 0.05$.

Study Approval

All animal protocols and experimental procedures were approved by the Institutional Animal Care and Use Committee at the University of Colorado-Denver.

REFERENCES

- Bassett, A.R., Tibbit, C., Ponting, C.P., and Liu, J.L. (2013). Highly efficient targeted mutagenesis of *Drosophila* with the CRISPR/Cas9 system. *Cell Rep* 4, 220-228.
- Hara, T., Nakamura, K., Matsui, M., Yamamoto, A., Nakahara, Y., Suzuki-Migishima, R., Yokoyama, M., Mishima, K., Saito, I., Okano, H., *et al.* (2006). Suppression of basal autophagy in neural cells causes neurodegenerative disease in mice. *Nature* 441, 885-889.
- Itakura, E., and Mizushima, N. (2010). Characterization of autophagosome formation site by a hierarchical analysis of mammalian Atg proteins. *Autophagy* 6, 764-776.
- Kohno, S., Shiozaki, Y., Keenan, A.L., Miyazaki-Anzai, S., and Miyazaki, M. (2019). An N-terminal-truncated isoform of FAM134B (FAM134B-2) regulates starvation-induced hepatic selective ER-phagy. *Life Sci Alliance* 2.

- Li, J., Casteels, T., Frogne, T., Ingvorsen, C., Honore, C., Courtney, M., Huber, K.V.M., Schmitner, N., Kimmel, R.A., Romanov, R.A., *et al.* (2017). Artemisinin Target GABAA Receptor Signaling and Impair alpha Cell Identity. *Cell* 168, 86-100 e115.
- Man, W.C., Miyazaki, M., Chu, K., and Ntambi, J. (2006). Colocalization of SCD1 and DGAT2: implying preference for endogenous monounsaturated fatty acids in triglyceride synthesis. *J Lipid Res* 47, 1928-1939.
- Masuda, M., Miyazaki-Anzai, S., Keenan, A.L., Okamura, K., Kendrick, J., Chonchol, M., Offermanns, S., Ntambi, J.M., Kuro, O.M., and Miyazaki, M. (2015). Saturated phosphatidic acids mediate saturated fatty acid-induced vascular calcification and lipotoxicity. *J Clin Invest* 125, 4544-4558.
- Masuda, M., Miyazaki-Anzai, S., Keenan, A.L., Shiozaki, Y., Okamura, K., Chick, W.S., Williams, K., Zhao, X., Rahman, S.M., Tintut, Y., *et al.* (2016). Activating transcription factor-4 promotes mineralization in vascular smooth muscle cells. *JCI Insight* 1, e88646.
- Masuda, M., Miyazaki-Anzai, S., Levi, M., Ting, T.C., and Miyazaki, M. (2013). PERK-eIF2alpha-ATF4-CHOP signaling contributes to TNFalpha-induced vascular calcification. *J Am Heart Assoc* 2, e000238.
- Masuda, M., Ting, T.C., Levi, M., Saunders, S.J., Miyazaki-Anzai, S., and Miyazaki, M. (2012). Activating transcription factor 4 regulates stearate-induced vascular calcification. *J Lipid Res* 53, 1543-1552.
- Miyazaki-Anzai, S., Levi, M., Kratzer, A., Ting, T.C., Lewis, L.B., and Miyazaki, M. (2010). Farnesoid X receptor activation prevents the development of vascular calcification in ApoE^{-/-} mice with chronic kidney disease. *Circ Res* 106, 1807-1817.
- Miyazaki-Anzai, S., Masuda, M., Demos-Davies, K.M., Keenan, A.L., Saunders, S.J., Masuda, R., Jablonski, K., Cavaasin, M.A., Kendrick, J., Chonchol, M., *et al.* (2014). Endoplasmic reticulum stress effector CCAAT/enhancer-binding protein homologous protein (CHOP) regulates chronic kidney disease-induced vascular calcification. *J Am Heart Assoc* 3, e000949.
- Miyazaki, M., Flowers, M.T., Sampath, H., Chu, K., Otselberger, C., Liu, X., and Ntambi, J.M. (2007). Hepatic stearyl-CoA desaturase-1 deficiency protects mice from carbohydrate-induced adiposity and hepatic steatosis. *Cell Metab* 6, 484-496.
- Nagle, C.A., Vergnes, L., Dejong, H., Wang, S., Lewin, T.M., Reue, K., and Coleman, R.A. (2008). Identification of a novel sn-glycerol-3-phosphate acyltransferase isoform, GPAT4, as the enzyme deficient in *Agpat6*^{-/-} mice. *J Lipid Res* 49, 823-831.
- Nishimura, T., Tamura, N., Kono, N., Shimanaka, Y., Arai, H., Yamamoto, H., and Mizushima, N. (2017). Autophagosome formation is initiated at phosphatidylinositol synthase-enriched ER subdomains. *EMBO J* 36, 1719-1735.
- Rohatgi, R.A., Janusis, J., Leonard, D., Bellve, K.D., Fogarty, K.E., Baehrecke, E.H., Corvera, S.,

and Shaw, L.M. (2015). Beclin 1 regulates growth factor receptor signaling in breast cancer. *Oncogene* 34, 5352-5362.

Shiozaki, Y., Okamura, K., Kohno, S., Keenan, A.L., Williams, K., Zhao, X., Chick, W.S., Miyazaki-Anzai, S., and Miyazaki, M. (2018). The CDK9-cyclin T1 complex mediates saturated fatty acid-induced vascular calcification by inducing expression of the transcription factor CHOP. *J Biol Chem* 293, 17008-17020.

Uematsu, M., Nishimura, T., Sakamaki, Y., Yamamoto, H., and Mizushima, N. (2017). Accumulation of undegraded autophagosomes by expression of dominant-negative STX17 (syntaxin 17) mutants. *Autophagy* 13, 1452-1464.

Vergnes, L., Beigneux, A.P., Davis, R., Watkins, S.M., Young, S.G., and Reue, K. (2006). Agpat6 deficiency causes subdermal lipodystrophy and resistance to obesity. *J Lipid Res* 47, 745-754.

Wieckowski, M.R., Giorgi, C., Lebiedzinska, M., Duszynski, J., and Pinton, P. (2009). Isolation of mitochondria-associated membranes and mitochondria from animal tissues and cells. *Nat Protoc* 4, 1582-1590.

Zhong, Y., Morris, D.H., Jin, L., Patel, M.S., Karunakaran, S.K., Fu, Y.J., Matuszak, E.A., Weiss, H.L., Chait, B.T., and Wang, Q.J. (2014). Nrbf2 protein suppresses autophagy by modulating Atg14L protein-containing Beclin 1-Vps34 complex architecture and reducing intracellular phosphatidylinositol-3 phosphate levels. *J Biol Chem* 289, 26021-26037.

KEY RESOURCES TABLE

REAGENT or RESOURCE	SOURCE	IDENTIFIER
Antibodies		
Lc3 rabbit polyclonal (IF = 1:500)	MBL International	Cat#PM036
Lc3 mouse monoclonal (IF = 1:200)	MBL International	Cat#M152-3
Lc3 rabbit polyclonal (WB = 1:2000)	Novus Biologicals	Cat#NB100-2220
p62 (WB = 1:1000)	Cell Signaling Technology	Cat#5114
GAPDH (WB = 1:4000)	Santa Cruz Biotechnology	Cat#sc-20357
β -Actin (WB = 1:10000)	Proteintech	Cat#66009
ATG5 (WB = 1:1000)	Cell Signaling Technology	Cat# #12994
LAMP1 (WB = 1 μ g in 10ml, IF = 1:50)	Developmental Studies Hybridoma Bank	Cat#1D4B
EGFR (WB = 1:1000)	Cell Signaling Technology	Cat#4267
WIPI2 (IF = 1:100)	Sigma-Aldrich	Cat#SAB4200400
ATG16L1 (IF = 1:100)	Cell Signaling Technology	Cat#8089
ATF4 (WB = 1:1000)	Cell Signaling Technology	Cat#11815
CHOP (WB = 1:1000)	Cell Signaling Technology	Cat #2895
BiP (WB = 1:1000)	Cell Signaling Technology	Cat #3177
RCAS1 (WB = 1:1000, IF = 1:100)	Cell Signaling Technology	Cat#12290
Calnexin (WB = 1:10000, IF = 1:800)	Bethyl Laboratories	Cat# A303-696A
Tomm20 (WB = 1:2000, IF = 1:200)	Santa Cruz Biotechnology	Cat#sc-11415
KDEL 10C3 (IF = 1:100)	MBL international	Cat#SR-827
GFP (WB = 1:2000)	Santa Cruz Biotechnology	Cat#sc-9996
Beclin (WB = 1:1000)	Cell Signaling Technology	Cat #3495
PI3 Kinase Class III (WB = 1:1000)	Cell Signaling Technology	Cat #4263
Syntaxin-17 (WB = 1:1000)	Bethyl Laboratories	Cat#A305-750A
Facl4 (WB = 1:1000)	Novus Biologicals	Cat#NBP2-16401
Agpat6 (Gpat4) (WB = 1:1000)	Proteintech	Cat#16762-1-AP
FLAG M2 (IF = 1:200)	Sigma-Aldrich	Cat# F1804
Caspase-3 (WB = 1:1000)	Cell Signaling Technology	Cat#9662
Fam134b (WB = 1:1000)	(Kohno et al., 2019)	N/A
Testis expressed 264 (Tex264) (WB = 1:1000)	Novus Biologicals	Cat#NBP1-89866
Alexa Fluor 488-conjugated anti-rabbit IgG	Thermo Fisher Scientific	Cat#A-11034
Alexa Fluor 568-conjugated anti-rabbit IgG	Thermo Fisher Scientific	Cat#A-11011
Alexa Fluor 660-conjugated anti-rabbit IgG	Thermo Fisher Scientific	Cat#A-21074

Alexa Fluor 568-conjugated anti-mouse IgG	Thermo Fisher Scientific	Cat#A-11004
Alexa Fluor 568-conjugated anti-rat IgG	Thermo Fisher Scientific	Cat#A-11077
HRP-conjugated goat polyclonal anti-rabbit IgG	Thermo Fisher Scientific	Cat#31460
HRP-conjugated goat polyclonal anti-mouse IgG	Thermo Fisher Scientific	Cat#31430
HRP-conjugated rabbit polyclonal anti-rat IgG	Sigma-Aldrich	Cat#A5795
Chemicals, Peptides, and Recombinant Proteins		
Tamoxifen	TCI America	Cat#T2510
In Situ Cell Death Detection Kit	Roche	Cat#11684795910
TurboFect Transfection Reagent	Thermo Fisher Scientific	Cat#R0531
Lipofectamine RNAiMAX	Thermo Fisher Scientific	Cat#13778150
Polybrene	Sigma-Aldrich	Cat#TR-1003
DMEM	Thermo Fisher Scientific	Cat#12800017
FBS	Thermo Fisher Scientific	Cat#10437028
Penicillin/streptomycin	CORNING	Cat#30-002-CI
Trypsin	Sigma-Aldrich	Cat#T4674-
EBSS	Sigma-Aldrich	Cat#E2888
Poly-L-Lysine	R&D systems	Cat#3438-100-01
OPTI-MEM	Thermo Fisher Scientific	Cat#51985034
MeltDoctor™ HRM Master Mix	Thermo Fisher Scientific	Cat#4415440
SYBR™ Select Master Mix	Thermo Fisher Scientific	Cat#4472908
Leupeptin	GOLDBIO	Cat#L-010-5
Pepstatin A	GOLDBIO	Cat#P-020-5
Bafilomycin A1	Cayman Chemical	Cat#11038
CAY10566	Cayman Chemical	Cat#10012562
Triacsin C	Cayman Chemical	Cat#10007448
Brp-LPA	Echelon Biosciences	Cat# L-7416
AM095	APExBIO	Cat#A3166
H2L5186303	APExBIO	Cat#B5748
SAR405	APExBIO	Cat#A8883
50%Optiprep	Sigma-Aldrich	Cat#1114542
Percoll density gradient media	GE Healthcare Life Sciences	Cat#17089102
HCS LipidTOX™ Red Neutral Lipid Stain	Thermo Fisher Scientific	Cat#H34476
PI(3)P Mass ELISA	Echelon Biosciences	Cat#K-3300

High-Capacity cDNA Reverse Transcription Kit	Applied Biological Materials Inc.	Cat# 4368814
Epidermal growth factor	GOLDBIO	Cat#1350-04-100
VECTASHIELD® Antifade Mounting Medium with DAPI	VECTOR LABORATORIES	Cat#H-1200
Digitonin	Sigma-Aldrich	Cat#D141
Gelatin	Sigma-Aldrich	Cat#G7041
Glycine	Thermo Fisher Scientific	Cat#BP3815
Paraformaldehyde	Electron Microscopy Sciences	Cat#15710
Saponin	Sigma-Aldrich	Cat#S4521
Bovine Serum Albumin (BSA), Fraction V, Fatty Acid Free	GOLDBIO	Cat#A-421-10
16:0	NU-CHEK PREP, INC.	Cat#N-16-A
16:1 (n-7)	NU-CHEK PREP, INC.	Cat#U-40-A
18:0	NU-CHEK PREP, INC.	Cat#N-18-A
18:1 (n-9)	NU-CHEK PREP, INC.	Cat#U-46-A
18:1 (n-7)	NU-CHEK PREP, INC.	Cat#U-48-A
18:2 (n-6)	NU-CHEK PREP, INC.	Cat#U-60-A
18:3 (n-3)	NU-CHEK PREP, INC.	Cat#U-62-A
18:3 (n-6)	NU-CHEK PREP, INC.	Cat#U-63-A
20:0	NU-CHEK PREP, INC.	Cat#N-20-A
20:1 (n-9)	NU-CHEK PREP, INC.	Cat#U-66-A
20:3 (n-3)	NU-CHEK PREP, INC.	Cat#U-70-A
20:4 (n-6)	NU-CHEK PREP, INC.	Cat#U-71-A
20:5 (n-3)	NU-CHEK PREP, INC.	Cat#U-99-A
22:1 (n-9)	NU-CHEK PREP, INC.	Cat#U-79-A
22:6 (n-3)	NU-CHEK PREP, INC.	Cat#U-84-A
17:0-LPA	Avanti Polar Lipids	Cat#857127
18:0-LPA	Avanti Polar Lipids	Cat#857128
18:1-LPA	Avanti Polar Lipids	Cat#857130
18:0/18:0-PA	Avanti Polar Lipids	Cat#830865
18:1/18:1-PA	Avanti Polar Lipids	Cat#840875
Experimental Models: Cell Lines		
Mouse VSMCs (MOVAS-1)	ATCC	Cat#CRL-2797™

Human VSMCs (hAoSMC)	Applied Biological Materials Inc.	Cat#T0515
HeLa	ATCC	Cat#CCL-2™
NIH3T3	ATCC	Cat#CRL-1658™
HEK293T	ATCC	Cat#CRL-3216™
MOVAS-1 (GFP-p62)	This paper	N/A
MOVAS-1 (Atg5 KO)	This paper	N/A
MOVAS-1 scrambled sg	This paper	N/A
MOVAS-1 (stable GFP-LC3-RFP-LC3ΔG)	This paper	N/A
MOVAS-1 (stable GFP-STX17)	This paper	N/A
MOVAS-1 (stable GFP-DFCP1)	This paper	N/A
MOVAS-1 (Empty shRNA)	(Masuda et al., 2015)	N/A
MOVAS-1 (Acat1 shRNA)	(Masuda et al., 2015)	shRNA clone ID; V2LMM_34791
MOVAS-1 (Acat2 shRNA)	(Masuda et al., 2015)	shRNA clone ID; V3LMM_423666
MOVAS-1 (Agpat1 shRNA)	(Masuda et al., 2015)	shRNA clone ID; TRCN0000173860
MOVAS-1 (Agpat2 shRNA)	(Masuda et al., 2015)	shRNA clone ID; V2LMM_64946
MOVAS-1 (Agpat3 shRNA)	(Masuda et al., 2015)	shRNA clone ID; V3LMM_460834
MOVAS-1 (Agpat4 shRNA)	(Masuda et al., 2015)	shRNA clone ID; V3LMM_446166
MOVAS-1 (Agpat5 shRNA)	(Masuda et al., 2015)	shRNA clone ID; V3LMM_415929
MOVAS-1 (Dgat1 shRNA)	(Masuda et al., 2015)	shRNA clone ID; TRCN0000124789
MOVAS-1 (Dgat2 shRNA)	(Masuda et al., 2015)	shRNA clone ID; TRCN0000125476
MOVAS-1 (Gpat1 shRNA)	(Masuda et al., 2015)	shRNA clone ID; TRCN0000012156
MOVAS-1 (Gpat3 shRNA)	(Masuda et al., 2015)	shRNA clone ID; TRCN0000099285

MOVAS-1 (<i>Gpat4</i> shRNA)	(Masuda et al., 2015)	shRNA clone ID; V3LMM_414952
MOVAS-1 (<i>Lpcat1</i> shRNA)	(Masuda et al., 2015)	shRNA clone ID; TRCN0000183242
MOVAS-1 (<i>Lpcat2</i> shRNA)	(Masuda et al., 2015)	shRNA clone ID; V3LMM_508093
MOVAS-1 (<i>Lpcat3</i> shRNA)	(Masuda et al., 2015)	shRNA clone ID; V3LMM_511114
MOVAS-1 (<i>Lpcat4</i> shRNA)	(Masuda et al., 2015)	shRNA clone ID; V3LMM_451294
MOVAS-1 (<i>Lpgat1</i> shRNA)	(Masuda et al., 2015)	shRNA clone ID; TRCN0000125609
MOVAS-1 (<i>Mboat1</i> shRNA)	(Masuda et al., 2015)	shRNA clone ID; V3LMM_510216
MOVAS-1 (<i>Mboat2</i> shRNA)	(Masuda et al., 2015)	shRNA clone ID; TRCN0000018442
MOVAS-1 (<i>Sptlc1</i> shRNA)	(Masuda et al., 2015)	shRNA clone ID; TRCN0000103400
MOVAS-1 (GFP-DFCP1/FLAG-GPAT4-tdTomato)	This paper	N/A
Experimental Models: Organisms/Strains		
DBA/2J	The Jackson Laboratory	Cat#000671
<i>SMC-Scd1/2</i> KO DBA/2J	(Masuda et al., 2015)	N/A
<i>SMMHC-CreER^(T2)</i>	(Wirth et al., 2008)	N/A
<i>Atg5</i> (lox/lox)	(Hara et al., 2006)	N/A
<i>SMMHC-CreER^(T2); Atg5</i> (lox/lox) DBA/2J	This paper	N/A
<i>Gpat4</i> KO	(Vergnes et al., 2006)	N/A
<i>SMC-Scd1/2</i> KO; <i>Gpat4</i> KO DBA/2J	This paper	N/A
Recombinant DNA and siRNA oligonucleotides		
pLenti-U6-sgRNA-SFFV-Cas9-2A-Puro <i>Atg5</i> target 1 sequence; CTTCGAGATGTGTGGTT	Applied Biological Materials Inc.	Cat#K4591606
pLenti-U6-sgRNA-SFFV-Cas9-2A-Puro Scrambled sgRNA	Applied Biological Materials Inc.	Cat#K010
pMRX-IP-GFP-LC3-RFP-LC3ΔG	Dr. Noboru Mizushima (Kaizuka et al., 2016)	Addgene Cat#84572
pMXs-puro GFP-p62	Addgene	Cat#38277

pMRX-IP GFP-Stx17 WT	Addgene	Cat#45909
pMXs-puro GFP-DFCP1	Addgene	Cat#38269
Plenti CMV FLAG-GPAT4-tdTomato	This paper	N/A
psPAX2	Addgene	Cat#12260
pMD2	Addgene	Cat#12259
pUMVC	Addgene	Cat#8449
pCMV-VSV-G	Addgene	Cat# 8454
pcDNA4-VPS34-FLAG	Addgene	Cat #24398
Negative Control siRNA	Thermo Fisher Scientific	Cat#4390844
Mtm1 siRNA	Dharmacon	Cat# L-040161-00
Mtmr1 siRNA	Dharmacon	Cat# L-045040-00
Mtmr2 siRNA	Dharmacon	Cat# L-050609-00
Mtmr3 siRNA	Dharmacon	Cat# L-040547-02
Mtmr4 siRNA	Dharmacon	Cat# L-040162-00
Mtmr5 (Sbf1) siRNA	Dharmacon	Cat# L-048933-00
Mtmr6 siRNA	Dharmacon	Cat# L-061169-00
Mtmr7 siRNA	Dharmacon	Cat# L-046075-00
Mtmr9 siRNA	Dharmacon	Cat# L-057307-00
Mtmr10 siRNA	Dharmacon	Cat# L-055195-01
Mtmr11 siRNA	Dharmacon	Cat# L-058360-01
Mtmr12 siRNA	Dharmacon	Cat# L-059569-01
Mtmr13 (Sbf2) siRNA	Dharmacon	Cat# L-058020-00
Mtmr14 siRNA	Dharmacon	Cat# L-050513-01
Agpat6 (Gpat4) siRNA (ID s97917)	Thermo Fisher Scientific	Cat#4390771
Oligonucleotides		
18S rRNA: CGCCGCTAGAGGTGAAATTCT	(Masuda et al., 2015)	N/A
18S rRNA: CGAACCTCCGACTTTCGTTCT	(Masuda et al., 2015)	N/A
Mtm1: GGTTCCTATCGGACCTCAGAT	This paper	N/A
Mtm1 CCACTCATACCGACAAGAGGCT	This paper	N/A
Mtmr1: TGTGGATGGGACACATTGGCTG	This paper	N/A
Mtmr1: GCAGTGGATGACCACGGAAGTT	This paper	N/A
Mtmr2: CCTCTTGTTGTGCCAGCAAAC	This paper	N/A
Mtmr2: AGCGAGTGACTGTGGCTTGACT	This paper	N/A
Mtmr3: AGCAGACTCAGGAACGGACATG	This paper	N/A
Mtmr3: TCAGATTCCGCACATGGCACAC	This paper	N/A

Mtmr4: CTGTGTTCTCCAGTGGCTTGA	This paper	N/A
Mtmr4: CCAGGAATGTGCCGTAGAGACA	This paper	N/A
Sbf1 (Mtmr5): ACATACCGCGTCATCTTCACGG	This paper	N/A
Sbf1 (Mtmr5): GTCTGCACACTAATGCGCTTCTC	This paper	N/A
Mtmr6: CTTGGCAACTGTCAGAAGGAGAG	This paper	N/A
Mtmr6: TGGCTCCAAGACTGTCAGTCTC	This paper	N/A
Mtmr7: TAGCCAGAAGGAGAGGCGAGAA	This paper	N/A
Mtmr7: AGCTGTAGGCAGATGAAGGCTC	This paper	N/A
Mtmr9: AGGTGGCTTTGAACAGGAGGCT	This paper	N/A
Mtmr9: CCACGAGTTTGATTAGGCTCTCC	This paper	N/A
Mtmr10: GCAACCACTTGAAGAGGTCAGAG	This paper	N/A
Mtmr10: GCTGTCACACAGCACTGCTAAG	This paper	N/A
Mtmr11: ATGGCTCTCAGCCTTGGAAGGA	This paper	N/A
Mtmr11: CTTGGAGCACTACAGAACGGAC	This paper	N/A
Mtmr12: TGAAGGCTACCGAGTCTCTGAC	This paper	N/A
Mtmr12: CATTGTGACAGGACCAACACCAG	This paper	N/A
Sbf2 (Mtmr13): TACTTGCAAGCCTTATTGACTGC	This paper	N/A
Sbf2 (Mtmr13): TACCCATGCACTGGGGACAG	This paper	N/A
Mtmr14: AAGCCTGCTGAGATCCTCTACC	This paper	N/A
Mtmr14: TCAGGCAGAACTCTTCGGAGGT	This paper	N/A
Gpat4: AGCTTGATTGTCAACCTCCTG	(Masuda et al., 2015)	N/A
Gpat4: CCGTTGGTGTAGGGCTTGT	(Masuda et al., 2015)	N/A
Software and Algorithms		
High Resolution Melt Software Version 3.0.1	Applied Biosystems™	Cat#4461357
ImageJ2	NIH	https://imagej.net/ Welcome
Prism Version 5.00	GraphPad	N/A
FV10-ASW 4.2 Viewer	Olympus	N/A
Photoshop CS6	Adobe Systems	N/A

LEAD CONTACT AND MATERIALS AVAILABILITY

Lead contact, Makoto Miyazaki (Makoto.Miyazaki@CUANSCHUTZ.EDU)

Table S1. Enlarged omegasome in VPS34-FLAG overexpressed or Mtmr genes knockdown VSMCs expressing GFP-DFCP1, Related to Figure 3

	Percentage of VSMCs with enlarged GFP-DFCP1 structure	± SEM	siRNA Knockdown efficiency (Relative value against control siRNA)
Veh	2.67	2.67	N/A
C18:0	90.67*	1.33	N/A
Control Vec.	0.00	0.00	N/A
VPS34-FLAG	0.00	0.00	N/A
Negative control siRNA	2.67	1.33	1
Mtm1 siRNA	1.33	1.33	0.42
Mtmr1 siRNA	1.33	1.33	0.36
Mtmr2 siRNA	0.00	0.00	0.31
Mtmr3 siRNA	2.67	2.67	0.44
Mtmr4 siRNA	4.00	0.00	0.33
Sbf1 (Mtmr5) siRNA	1.33	1.33	0.26
Mtmr6 siRNA	0.00	0.00	0.29
Mtmr7 siRNA	1.33	1.33	0.16
Mtmr9 siRNA	2.67	2.67	0.33
Mtmr10 siRNA	0.00	0.00	0.22
Mtmr11 siRNA	0.00	0.00	0.42
Mtmr12 siRNA	0.00	0.00	0.29
Sbf2 (Mtmr13) siRNA	2.67	1.33	0.26
Mtmr14 siRNA	0.00	0.00	0.31

Percentage of VSMCs with enlarged GFP-DFCP1 structures from Figure S4D and S4E analysis (n=3, from 25 cells in each experiment, One-way ANOVA). * $P < 0.05$ vs. vehicle (Veh). There was no significant difference between control, VPS34 overexpressed and all Mtmr si groups. To evaluate knockdown efficiency, qRT-PCR was performed with cDNA samples from VSMCs transfected with siRNA.

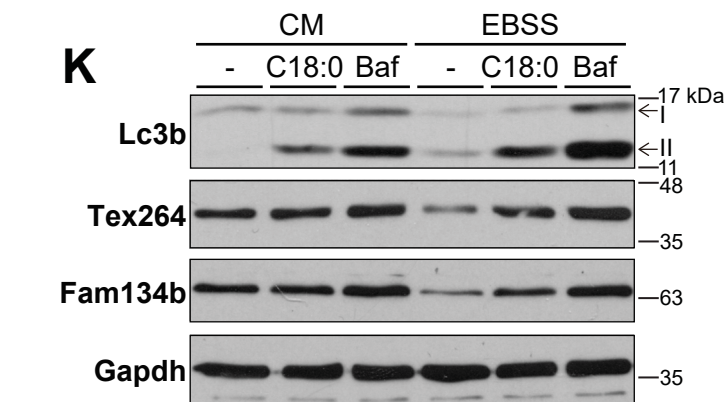
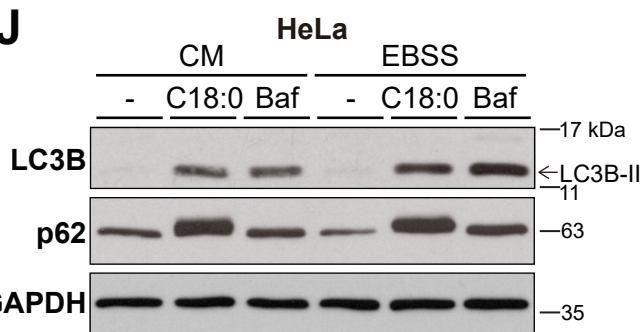
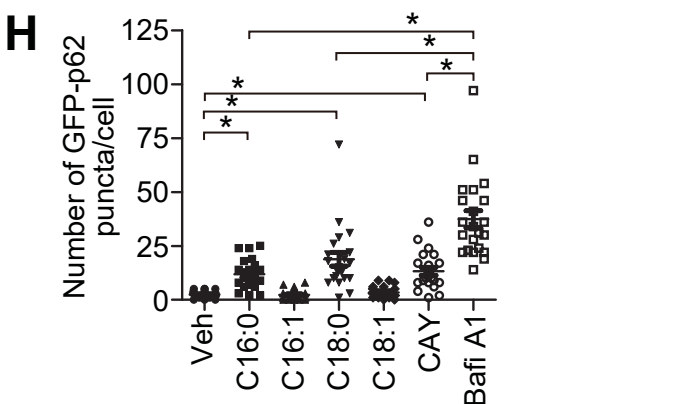
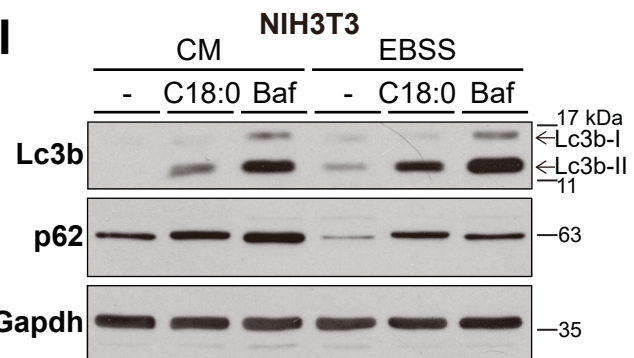
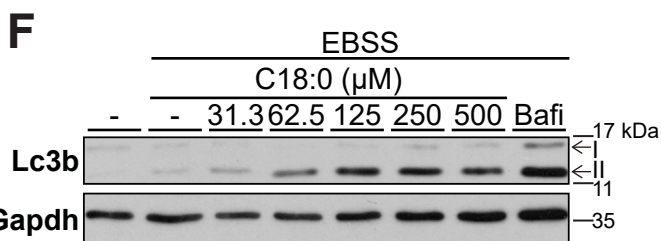
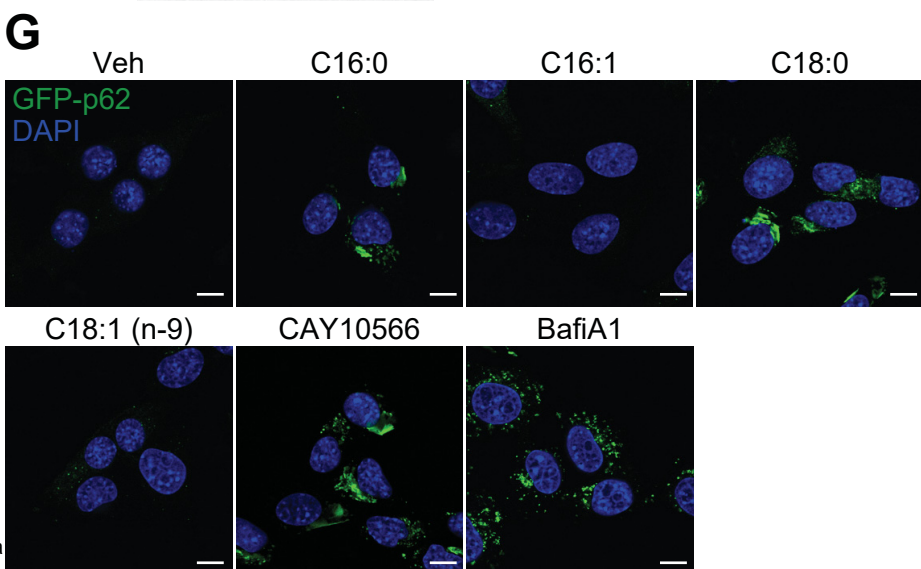
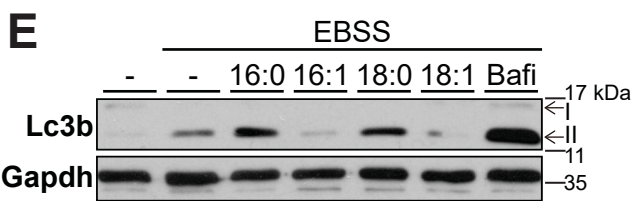
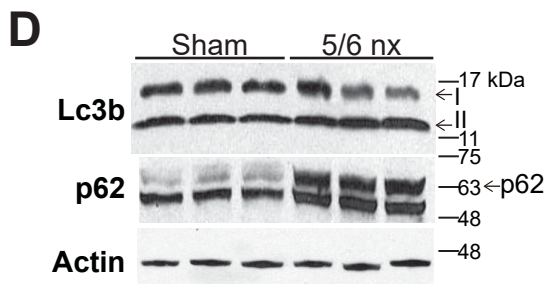
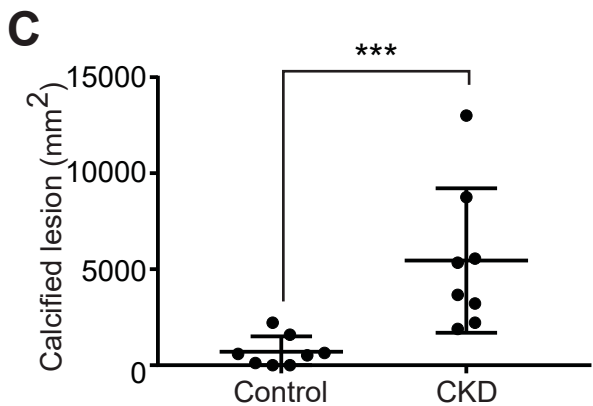
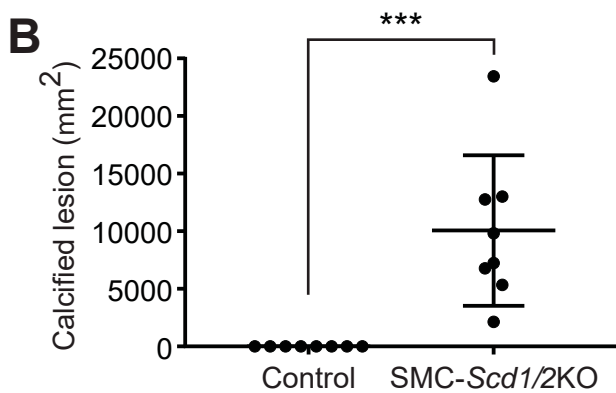
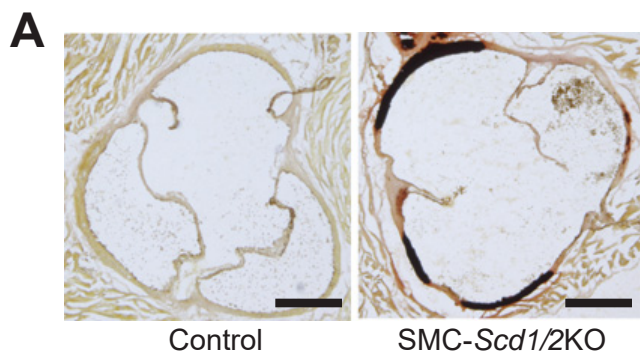


Figure S1. SFA inhibited autophagy in mouse aortas, NIH3T3 cells and HeLa cells, Related to Figure 1. (A) Photograph (x10 magnification) of the lesions in aortic sinuses stained with von Kossa in control and SMC-*Scd1/2* KO mice. Scale indicates 200 μm . (B) Quantitative analysis of calcified lesions from Figure 1A analysis (n=8, 2-tailed Student's t test). $P < 0.001$. Data are represented as mean \pm SEM. (C) Calcified lesions in CKD mice. $P < 0.001$. (D) Immunoblot analysis of aortic medias from DBA2/J mice with sham operation or CKD. (E) Immunoblot analysis of VSMCs treated with EBSS and BSA (Veh), 250 μM C16:0, C16:1, C18:0, C18:1 or 200 nM bafilomycin A1 for 2 hours. (F) Dose-dependent effect of C18:0 on starvation-induced degradation of Lc3b-II. Immunoblot analysis of VSMCs treated with EBSS and C18:0 or bafilomycin A1 for 2 hours. (G) Confocal microscopy images of GFP-p62 (green) and DAPI (blue) in stable VSMCs expressing GFP-p62 treated with BSA (Veh), 200 μM C16:0, 200 μM C16:1, 200 μM C18:0, 200 μM C18:1, 3 μM CAY 10566 and 50 μM C18:0 (CAY) or 200 nM bafilomycin A1 for 6 hours. Scale indicates 10 μm . (H) Number of GFP-p62 punctation in GFP-p62 VSMCs (n=22, One-way ANOVA). $*P < 0.05$. Data are represented as mean \pm SEM. Immunoblot analysis of NIH3T3 cells (I) and HeLa cells (J) treated with complete media or EBSS and BSA (-), 250 μM C18:0 or bafilomycin A1 for 6 hours. (K) Immunoblot analysis of ER-phagy receptor proteins (Tex264 and Fam134b) in VSMCs treated with complete media or EBSS and BSA (-), 250 μM C18:0 or 200 nM bafilomycin A1 for 6 hours.

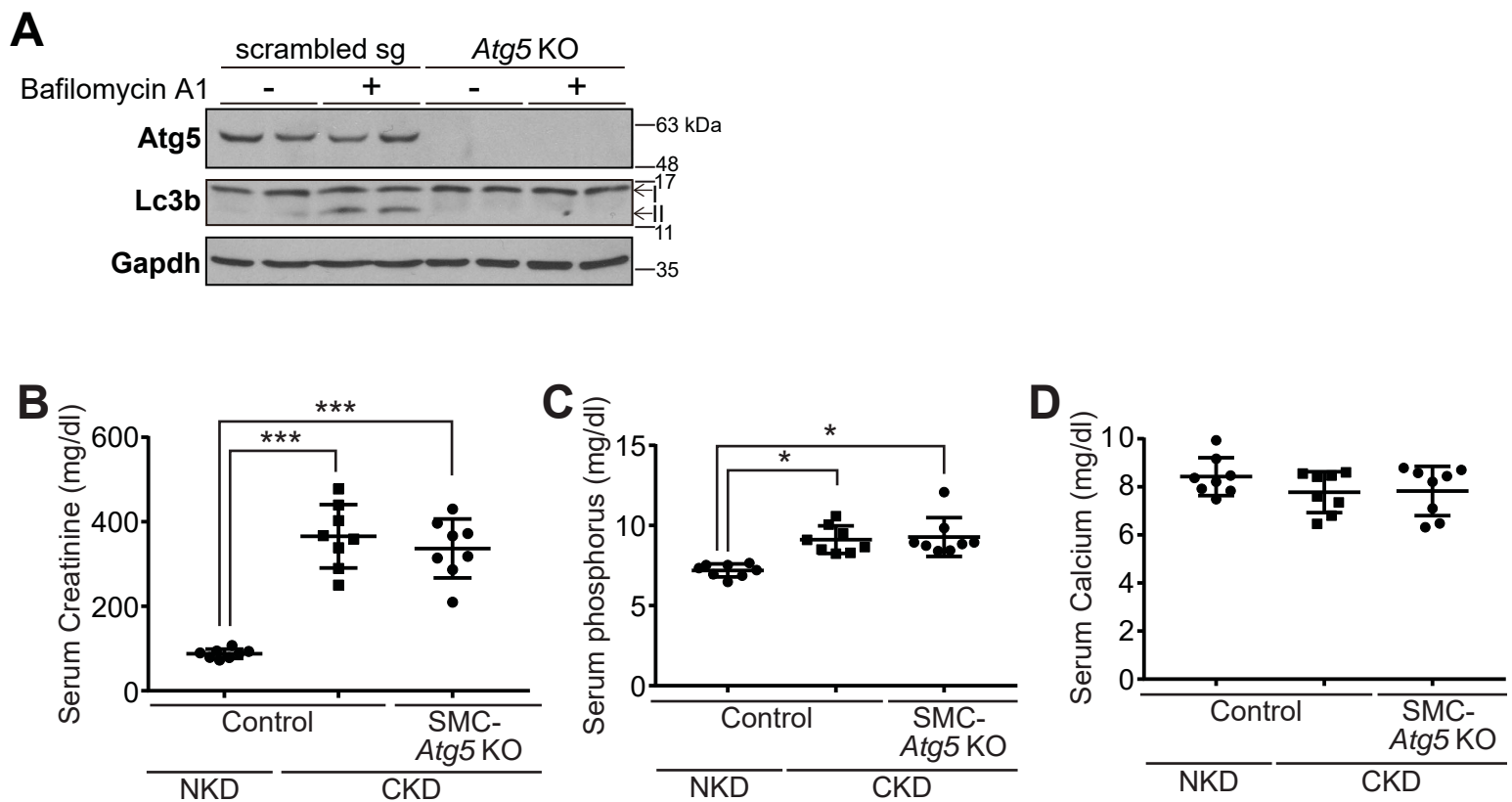


Figure S2. SMC-specific *Atg5* deficiency did not affect concentrations of serum creatinine, phosphate and calcium after 5/6 nephrectomy, Related to Figure 2.

(A) Immunoblot analysis of control (scrambled sg) or CRISPR-Cas9 based *Atg5* knockout (KO) VSMCs treated with DMSO (-) or 200 nM bafilomycin A1 for 6 hours. Levels of serum creatinine (B), phosphate (C) and calcium (D) in control and SMC-*Atg5* KO mice with sham-operation (NKD) or 5/6 nephrectomy (CKD) (n=8, One-way ANOVA). * $P < 0.05$, *** $P < 0.001$. Data are represented as mean \pm SEM.

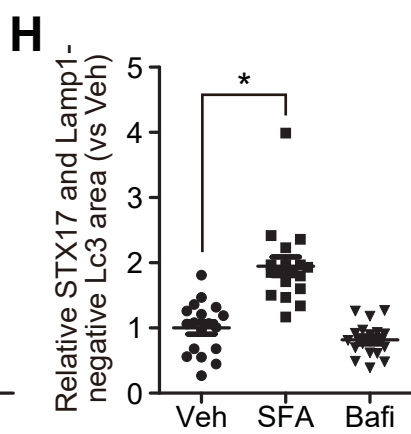
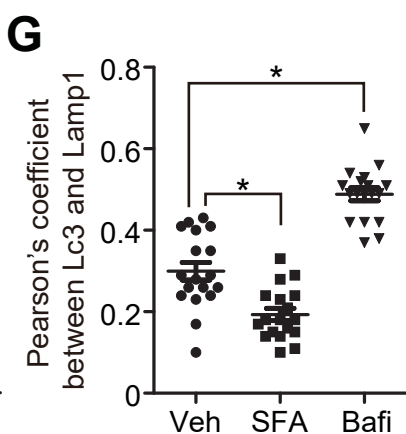
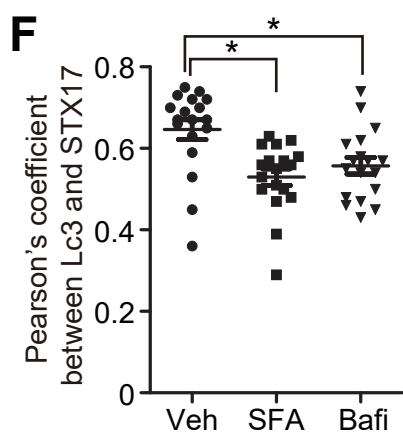
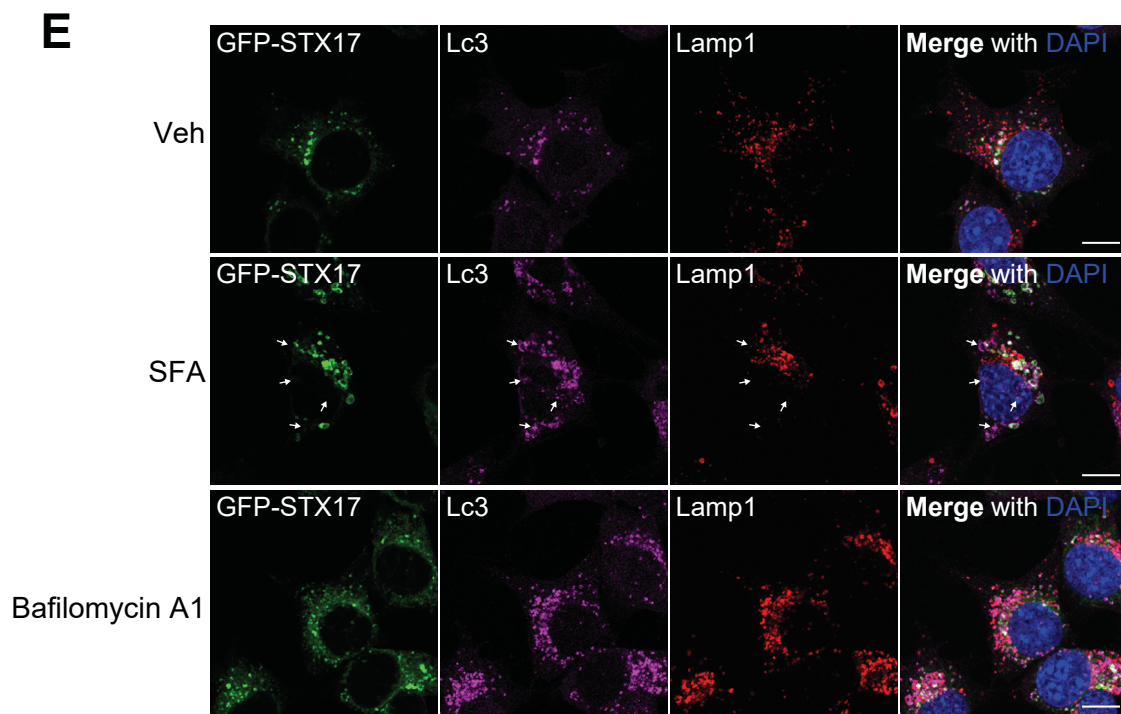
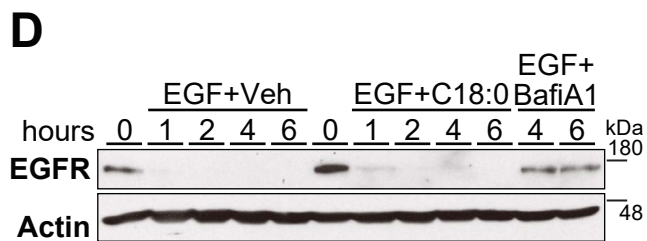
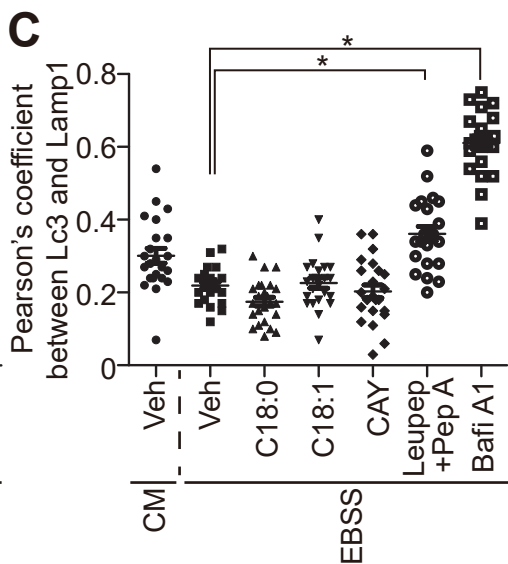
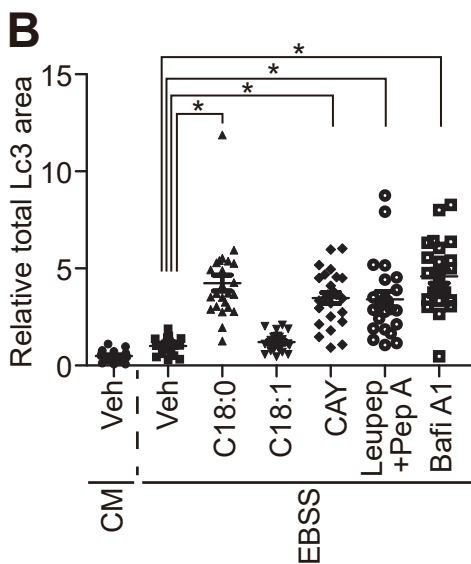
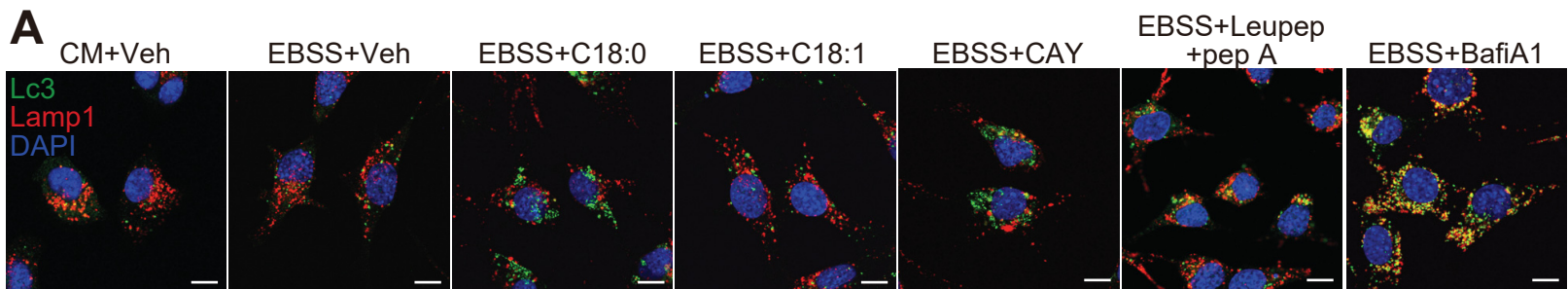


Figure S3. SFAs accumulated Lc3 prior to lysosomal degradation and mature autophagosome membrane formation in VSMCs, Related to Figure 3. (A) Immunofluorescence of Lc3 (green), Lamp1 (red) and DAPI (blue) in VSMCs were treated with complete media (CM) or EBSS and BSA (Veh), 200 μ M C18:0, 200 μ M C18:1, 3 μ M CAY10566 and 50 μ M C18:0 (CAY), 10 μ g/ml leupeptin and 10 μ g/ml pepstatin A (Leupep+pepA) or 200 nM bafilomycin A1 for 2 hours. Merge area (co-localization) between Lc3b and Lamp1 expressed as yellow color. Scale indicates 10 μ m. (B) Analysis of total Lc3 area in VSMCs (n=23–25, One-way ANOVA). * P <0.05. Data was expressed as fold value against EBSS Veh. (C) Pearson's coefficient between Lc3b and Lamp1 in VSMCs. (D) Immunoblot analysis of VSMCs treated with 10 nM EGF and BSA (EGF+Veh), EGF and 250 μ M C18:0 (EGF+C18:0) or EGF and 200 nM bafilomycin A1 (EGF+BafiA1) for 1, 2, 4 or 6 hours. (E) Confocal microscopy images of GFP-STX17 (green), Lc3 (magenta), Lamp1 (red) or DAPI (blue) in fixed stable VSMCs expressing GFP-STX17 treated with EBSS and BSA (veh), 200 μ M C18:0 (SFA) or 200 nM bafilomycin A1 for 2 hours. Scale indicates 10 μ m. White arrow in images of EBSS SFA indicates GFP-STX17 and Lamp1-double negative Lc3 area. Pearson's coefficient between Lc3 and GFP-STX17 images (F) or between Lc3 and Lamp1 images (G) (n=18, One-way ANOVA). * P <0.05. (H) Relative value of GFP-STX17 and Lamp1-double negative Lc3 area vs vehicle. Data are represented as mean \pm SEM.

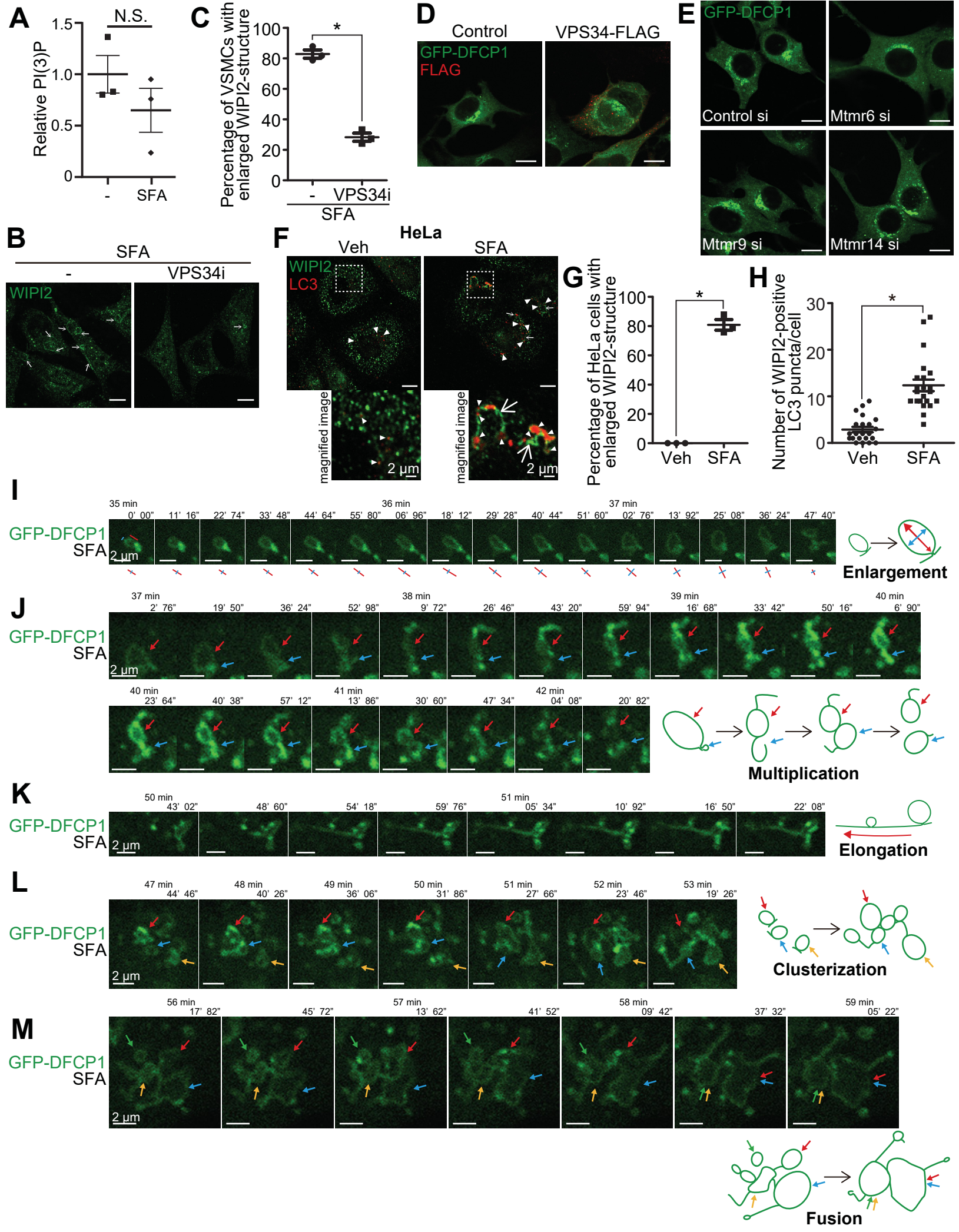


Figure S4. Characterization of SFA-induced abnormal formation of omegasomes, Related to Figure 3. (A) Levels of phosphatidylinositol 3-phosphate (PI3P) in VSMCs treated with 300 μ M C18:0 for 2 hours under starvation conditions using a PI3P ELISA kit. Total amount of PI3P was expressed as the relative value against control after adjustment by total amount of protein (n=3, 2-tailed Student's t test). N.S., Not Significant. (B) Confocal microscopy images of endogenous WIPI2 in VSMCs co-treated with 200 μ M C18:0 (SFA) and 10 μ M SAR405 (a VPS34 inhibitor) for 2 hours under EBSS conditions. Scale indicates 10 μ m and white arrow indicates enlarged WIPI2 structures. (C) Percentage of VSMCs with enlarged WIPI2 structures from Figure S4B analysis (n=3, from 33 cells in each experiment; 2-tailed Student's t test). * P <0.05. Data are represented as mean \pm SEM. (D) Confocal microscopy images of GFP-DFCP1 (green) and VPS34-FLAG (red) in stable VSMCs expressing GFP-DFCP1 that were transfected with control or VPS34-FLAG plasmid under 2 hours of starvation. Scale indicates 10 μ m. (E) Confocal microscopy images of GFP-DFCP1 (green) in stable VSMCs expressing GFP-DFCP1 that were transfected with 20 nM negative control, Mtmr6, Mtmr9 or Mtmr14 siRNA under 2 hours of starvation. Scale indicates 10 μ m. Mtm1, Mtmr1, Mtmr2, Mtmr3, Mtmr4, Sbf1 (Mtmr5), Mtmr7, Mtmr10, Mtmr11, Mtmr12 and Sbf2 (Mtmr13) knockdown did not induce abnormal omegasome formation (Table S1) (F) Confocal microscopy images of endogenous WIPI2 (green) and LC3 (red) in wild-type HeLa cells treated with EBSS and Veh or SFA for 2 hours. Scale indicates 10 μ m. Arrow indicates enlarged WIPI2 structures and arrowhead indicates WIPI2-positive Lc3. (G) Percentage of HeLa cells with enlarged WIPI2 structures (n=3, from 33 cells in each experiment; 2-tailed Student's t test). * P <0.05. Data are represented as mean \pm SEM. (H) Number of LC3 punctation with WIPI2 (n=22, 2-tailed Student's t test). * P <0.05. Data are represented as mean \pm SEM. (I–M) Dynamics of SFA-induced abnormal omegasome formation in VSMCs expressing GFP-DFCP1 from time lapse imaging of Supplemental Video 1. Time indicates time elapsed after SFA/EBSS treatment. (I) Enlargement: Red and blue line indicates omegasome diameter. (J) Multiplication: Omegasome (blue arrow) was duplicated/multiplied from the original omegasome (red). (K) Elongation of omegasome membrane. (L) Clusterization: multiple omegasomes (red, blue and orange arrows) clustered into one complex omegasome. (M) Fusion: After clusterization, multiple omegasome rings (red, blue, orange and green arrows) fused to generate a single large omegasome ring.

Figure S5. Localization of GFP-DFCP1 in VSMCs, Related to Figure 6. (A) Confocal microscopy images of RCAS1 (golgi, red), Calnexin (ER, red), Tomm20 (mitochondria, red) or Lamp1 (lysosome, red), GFP-DFCP1 (green) and DAPI (blue) in stable VSMCs expressing GFP-DFCP1 treated with EBSS and BSA (Veh) or C18:0 (SFA) for 2 hours. Arrowhead indicates enlarged GFP-DFCP1 structure and arrow indicates ER- or mitochondria-GFP-DFCP1 contact site. Scale indicates 10 μ m. (B) Confocal microscopy images of LipidTox (lipid droplet, red) and GFP-DFCP1 (green) in stable VSMCs expressing GFP-DFCP1 treated with EBSS and Veh or SFA for 2 hours. Arrowhead indicates enlarged GFP-DFCP1 structure. (C) Confocal microscopy images of Tomm20 (magenta), GFP-DFCP1 (green) or KDEL (red) in VSMCs treated with EBSS and BSA (Veh) or 200 μ M C18:0 (SFA) for 2 hours. Scale indicates 10 μ m. Arrow indicates Tomm20, GFP-DFCP1 and KDEL-all contact sites. (D) Number of GFP-DFCP1-KDEL-Tomm20 contacts site in Figure S5C analysis (n=16–17, 2-tailed Student's t test). * P <0.05. Data are represented as mean \pm SEM.

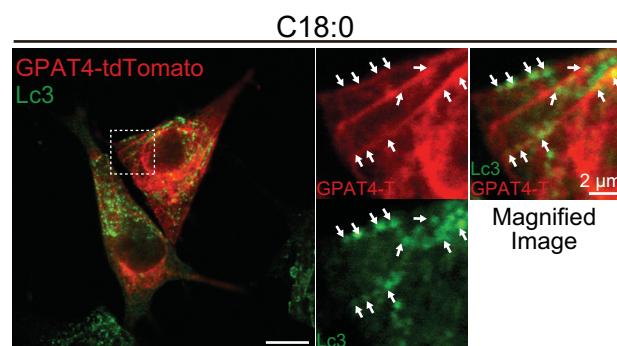
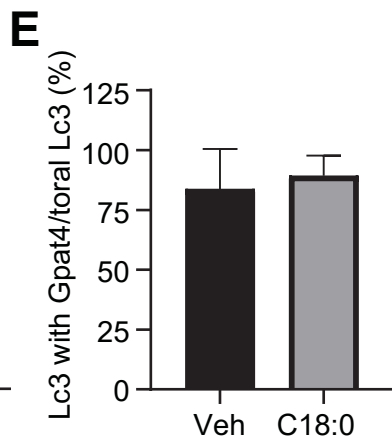
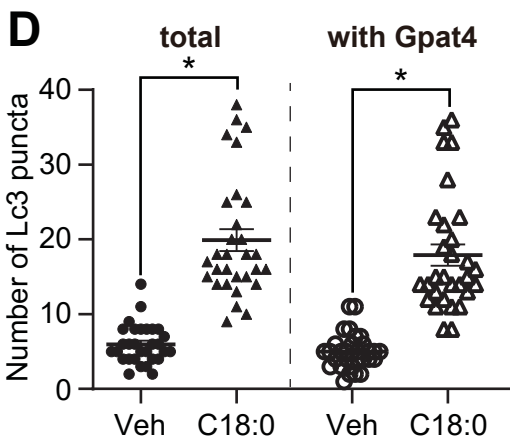
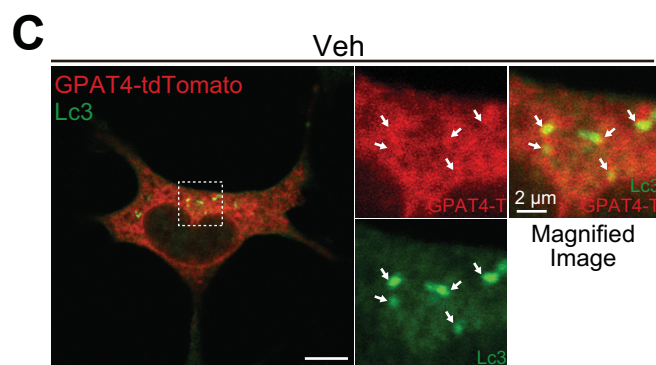
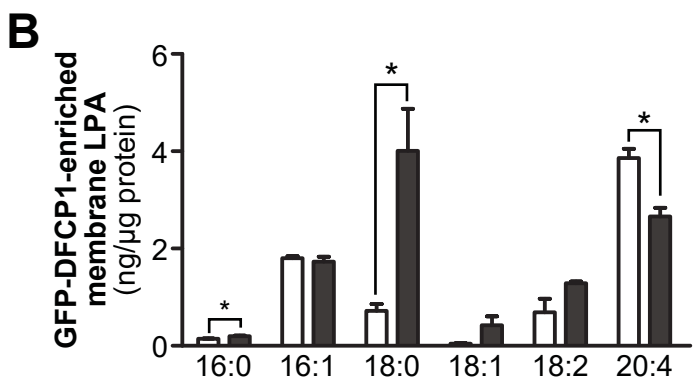
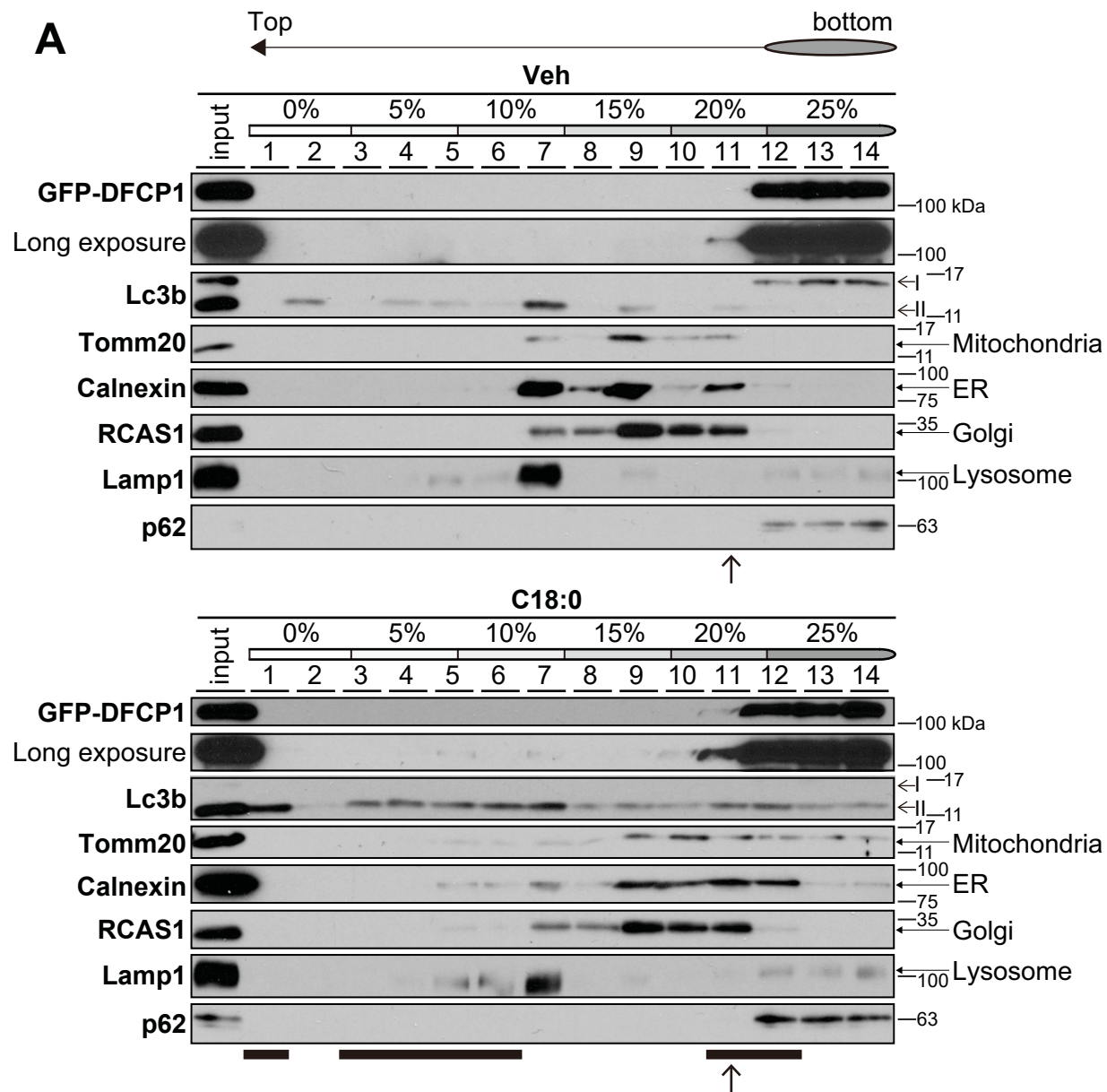


Figure S6. SFAs accumulated saturated LPAs in the fraction containing proteins of GFP-DFCP1, Lc3b-II, mitochondria and ER in VSMCs by Optiprep density centrifuge analysis, Related to Figure 6. (A) Immunoblot analysis of Optiprep density centrifuged fractions of VSMCs treated with EBSS and BSA (Veh) or C18:0 (SFA) for 2 hours. Bold black bars indicate where Lc3 increased fractions through treatment with SFAs compared to EBSS Veh. Arrow indicates fraction 11, which contains a GFP-DFCP1 protein-enriched membrane in SFA-treated VSMCs and was used for lysophosphatidic acid (LPA) analysis. (B) LC-MS-based absolute levels of LPA species in fraction 11 (n=3, 2-tailed Student's t test). * $P < 0.05$. Data are represented as mean \pm SEM. (C) Confocal microscopy images of Lc3 (green) and GPAT4-tdTomato (GPAT4-T) (red) in VSMCs stably expressing GPAT4-tdTomato that were treated with Veh or SFAs under EBSS conditions for 2 hours. Scale indicates 10 μ m. Arrow indicates Lc3 and GPAT4-tdTomato-contact sites. (D) Number of total Lc3 puncta and Lc3 puncta with GPAT4-tdTomato (n=30, 2-tailed Student's t test). * $P < 0.05$. Data are represented as mean \pm SEM. (E) Percentage of Lc3 puncta with GPAT4-tdTomato against total Lc3 puncta (n=30, 2-tailed Student's t test). Data are represented as mean \pm SEM.

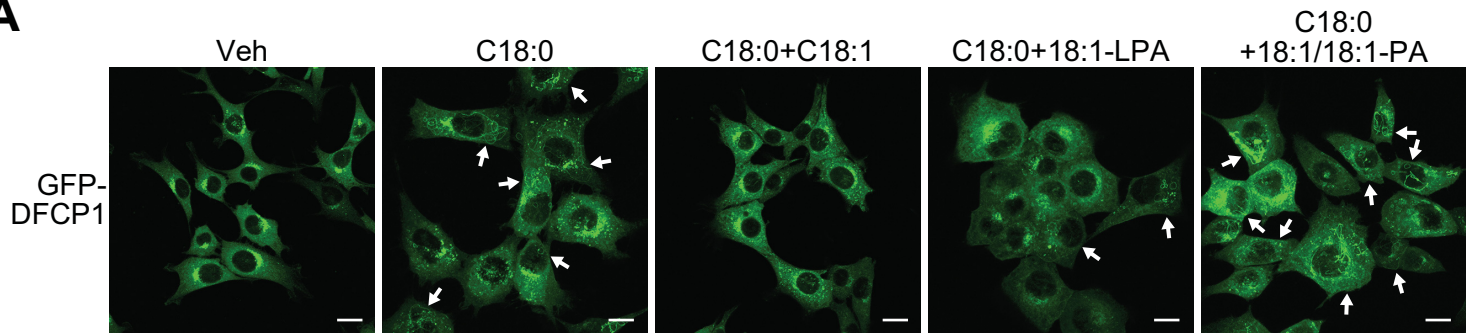
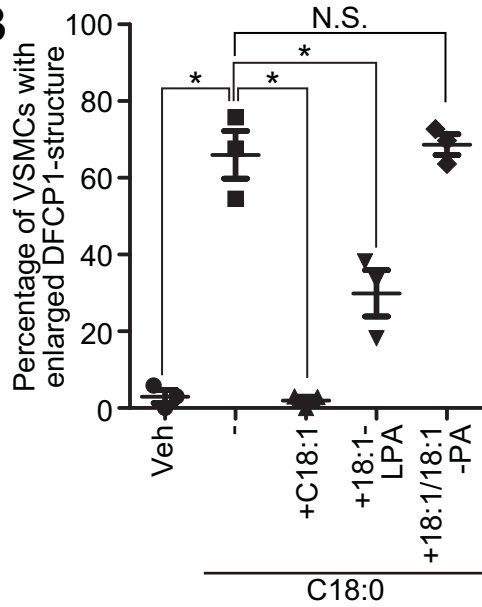
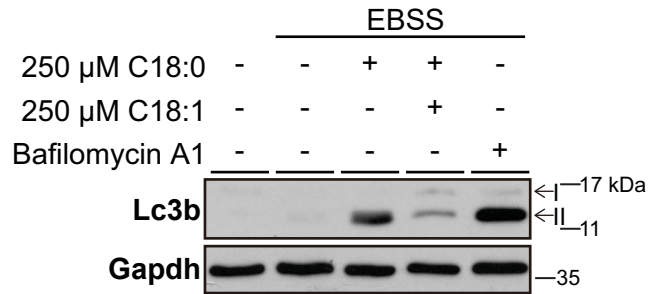
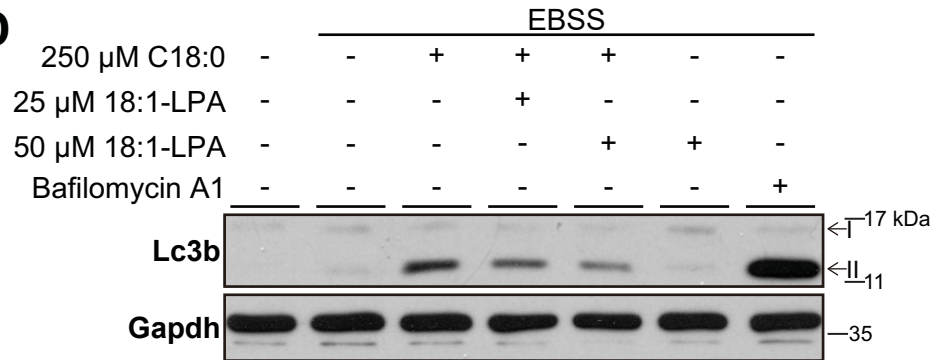
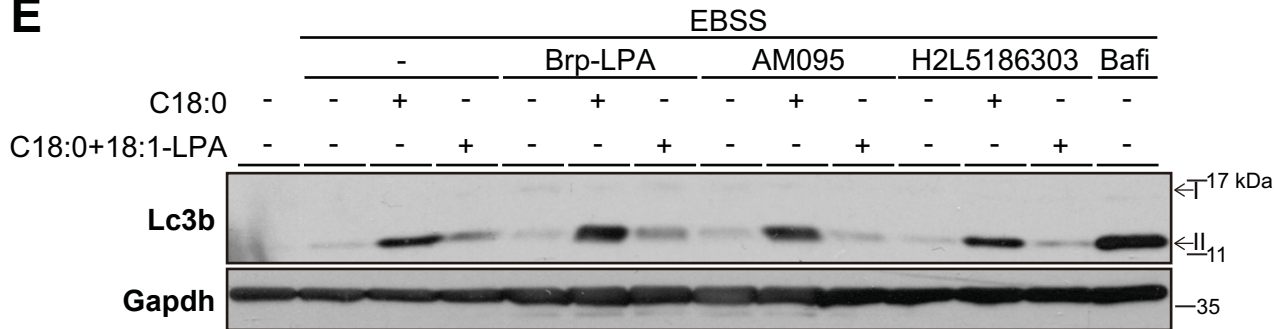
A**B****C****D****E**

Figure S7. Unsaturated fatty acids and unsaturated LPAs, but not unsaturated PAs, inhibited accumulation of lipidated Lc3 and enlarged GFP-DFCP1 omegasomes through SFA treatment in VSMCs, Related to Figure 8. (A) Confocal microscopy images in stable VSMCs expressing GFP-DFCP1 treated with EBSS and BSA (Veh), 200 μ M C18:0 and BSA, 200 μ M C18:0 and 200 μ M C18:1, 200 μ M C18:0 and 20 μ M 18:1-LPA or 200 μ M C18:0 and 20 μ M 18:1/18:1-PA for 2 hours. Scale indicates 20 μ m and arrow indicates VSMCs with enlarged GFP-DFCP1 structures. (B) Percentage of VSMCs with enlarged GFP-DFCP1 structures (n=3, from 30 cells in each experiment, One-way ANOVA). * P < 0.05; N.S., Not significant. Data are represented as mean \pm SEM. (C) Immunoblot analysis of VSMCs co-treated with EBSS and C18:0 and BSA (-), C18:0 and C18:1 or bafilomycin A1 for 2 hours. (D) Immunoblot analysis of VSMCs co-treated with EBSS and C18:0 and BSA, C18:0 and 18:1-LPA, BSA and 18:1-LPA or bafilomycin A1 for 2 hours. (E) Effect of LPA receptor inhibition on autophagy inhibition by SFAs and suppression of SFA-induced autophagy inhibition by unsaturated LPAs. Immunoblot analysis of VSMCs prepared as follows. VSMCs were pretreated with 10 μ M of an LPA receptor inhibitor (LPARi) such as Brp-LPA, AM095 or H2L5186303 for 2 hours, and then treated with EBSS and 250 μ M C18:0 and BSA (-), 250 μ M C18:0 and 25 μ M 18:1-LPA or bafilomycin A1 with or without 10 μ M LPARi for 2 hours.